Computational Mechanics (2021) 67:969–987
https://doi.org/10.1007/s00466-021-01978-7

ORIGINAL PAPER

Mesh size objective fatigue damage propagation in laminated composites using the multiscale discrete damage theory

Zimu Su[1] · **Caglar Oskay**[2]

Received: 21 June 2020 / Accepted: 24 January 2021 / Published online: 13 February 2021

Abstract
A mesh size objective multiscale modeling is developed for fatigue failure prediction of long fiber-reinforced composites based on the multiscale discrete damage theory (MDDT). MDDT tracks the failure processes along discrete failure surfaces at the microscale and concurrently bridges it to continuum-based description of damage at the macroscale. The proposed approach achieves mesh-size objectivity by introducing a length scale operator which effectively adjusts the microstructure size as a function of macroscale element size; and when a non-additive fatigue damage evolution law is used to describe progressive cracking at the microscale. Temporal multiscaling is used to track long-term fatigue damage evolution with high computational efficiency. The performance of the proposed model is demonstrated by the analysis of unnotched and open-hole laminate configurations. The results indicate mesh-size objectivity even in the presence of multiple failure mechanisms including splitting, delamination and transverse matrix cracks. The interaction between splitting and transverse cracks is investigated by a parametric study, which reveals the effects of mode I and mode II dominated degradation on the failure behavior under fatigue loading.

Keywords Multiscale modeling · Reduced order modeling · Fatigue · Composites laminates · Mesh-size objectivity

1 Introduction

Continuous fiber reinforced polymer composite materials typically exhibit favorable fatigue properties. Nevertheless, long-term fatigue degradation of composite structures remains to be a structural design consideration in aerospace, automobile and many other industries. The current design practices mostly rely on conservative knock-down factors to account for fatigue degradation. In contrast, ongoing research in modeling and prediction attempts to gain better understanding of fatigue failure mechanisms and facilitate damage tolerance principles to composite design. Early studies proposed accurate empirical or phenomenological fatigue theories for prediction of residual stiffness, residual strength and fatigue life of laminated composites (e.g. [1,2]). However, interactions between multiple failure modes associated with intralaminar/interlaminar damage in complex composite configurations are difficult to capture with analytical methods.

In the past decade or so, progressive damage analysis (PDA) has gained significant attention as a physics based framework for fatigue failure prediction of composites. Progressive damage analysis of composites subjected to fatigue have been performed based on either computational fracture mechanics or continuum damage mechanics approaches. Studies that couple Paris Law (or a variant) with J-integral, virtual crack extension and closure techniques (e.g. [3–5]) have been employed to study crack growth in composite laminates. These approaches are either combined with a crack nucleation model or restricted to configurations that include one or multiple precracks. They consider brittle crack growth with the assumption of negligible fracture process zone, which forms in quasi-brittle materials. Cohesive zone modeling (CZM) has also been used for fatigue crack prediction in composites. Most CZM-based studies focused on interlaminar failure (e.g. [6,7]) since most commonly used (intrinsic) CZM formulations require that the crack paths are pre-defined. Some studies also used CZM to describe intralaminar crack propagation [8–10] by placing cohesive

✉ Caglar Oskay
caglar.oskay@vanderbilt.edu

[1] Department of Civil and Environmental Engineering, Vanderbilt University, Nashville, TN 37235, USA

[2] VU Station B 351831, 2301 Vanderbilt Place, Nashville, TN 37235, USA

zone elements at all element faces. Element enrichment technologies such as the extended finite elements [11,12], the phantom node method [13] and the floating node method [5] have been recently employed as well. These methodologies allow cracks to grow along orientations independent of the finite element mesh.

Continuum damage mechanics (CDM) is also a common method for failure prediction of composites because of its simplicity and directness for computational implementation. A number of studies (e.g. [14–18]) focused on establishing cycle-sensitive damage evolution models to predict fatigue failure in composite materials. Cycle sensitive CDM models were then used to explore fatigue response of various composite configurations [19–21] under different fatigue loading conditions [22]. More recently, CDM-based multiscale models have been developed for fatigue damage and life prediction in composites. Arnold et al. [18] employed the Generalized Method of Cells accelerated with cycle jump approach. Oskay et al. proposed a multiscale spatial-temporal life prediction approach that relies on model order reduction in space [23–25] and time [26–29] to accelerate fatigue prediction. This approach has been applied to laminated open-hole as well as bolted joint composite configurations [30]. Regardless of whether the failure behavior is represented using single scale or multiscale models, CDM approaches exhibit spurious mesh sensitivity and lack of mesh convergence [31,32] due to damage localization. While this issue has been comprehensively studied for static loading over the past several decades, mesh sensitivity and alleviation strategies under fatigue loading conditions received relatively little attention. Only the nonlocal approach using gradient damage type [32] and integral type [33] localization limiters have been employed to achieve mesh-size objectivity in the fatigue case.

In this manuscript, we propose a mesh-size objective multiscale model for fatigue damage evolution and failure in composites. The proposed model builds on and generalizes the multiscale discrete damage theory (MDDT) that was recently proposed for composite failure under static loading conditions [25]. MDDT is a discrete-continuum multiscale approach, where the failure is tracked in discrete surfaces as fracture paths within the microstructure. Growth of the discrete microstructural fracture events culminates to diffuse damage patterns at the macroscopic scale, and hence exhibits mesh size sensitivity when unregularized. The proposed model achieves mesh-size objectivity at the coarse scale by adjusting the microstructure size in an effective manner with respect to the macroscopic element length using an analytically determined length scale parameter. In order to accelerate fatigue life predictions, the MDDT approach is integrated with a multiple time scaling approach [26,27]. We demonstrate that mesh size sensitivity of fatigue predictions can only be achieved when constitutive (i.e., traction-separation behavior) models with a specific form are used. The efficacy of the model is demonstrated in the context of un-notched and open-hole laminate configurations (0° ply and $[90^\circ/0^\circ]_S$ cross-ply) subjected to high-cycle fatigue loading. A parametric study is performed to explain the differences in fatigue crack patterns observed in composite laminates made of some thermoplastic and thermoset resins.

The rest of the manuscript is organized as follows: Sect. 2 provides a brief introduction of the multiscale discrete damage theory (MDDT) and temporal multiscale modeling, and also provides detailed information of mesh-size objectivity treatment and related fatigue cohesive model. Section 3 includes the verification of the proposed approach in the context of un-notched and open-hole laminated composite configurations, and provides a parametric study on the effect of mode-I and mode-II dominated fatigue failure behavior of composite laminates. Section 4 provides conclusions. The appendix includes additional details on multiple time scale modeling.

2 Multiscale discrete damage theory for fatigue

2.1 Spatial multiscale modeling

Progressive failure behavior in the composite material is modeled using the Multiscale Discrete Damage Theory (MDDT) recently proposed in Ref. [25]. A brief overview of MDDT and the governing equations are provided below. The underlying theory and detailed derivation of the governing equations are omitted herein for brevity.

The overall multiscaling strategy in MDDT is illustrated in Fig. 1. The proposed modeling approach relies on concurrent coupling between the scale of the composite microstructure (i.e., representative volume or unit cell) and the macroscopic domain using the computational homogenization theory [34,35]. The progressive failure process within the microstructure associated with an arbitrary position in the macroscale domain is modeled by tracking the cohesive (i.e., traction-separation) behavior over a pre-selected finite set of discrete "potential" failure paths (See Fig. 1b). Progressive fracture over each failure path is tracked throughout the loading process. The microscale response is bridged to the continuum representation of damage at the macroscopic scale based on averaging operations consistent with the mathematical homogenization theory [25]. In order to accelerate the analysis, the failure processes within the microstructure are computed using a reduced-order representation, with certain microstructural information precomputed (i.e., influence functions and coefficient tensors) prior to the macroscopic analysis. Although the macroscopic failure in MDDT is rep-

resented as continuum damage (i.e. smeared crack), MDDT differs from classical smeared crack models as it tracks discrete cracks within the microstructure. In addition, MDDT has the capability to incorporate multiple failure mechanisms at macroscale corresponding to failure paths embedded in the microstructure.

Consider a microstructure domain, Θ at an arbitrary macroscopic position $\mathbf{x} \in \Omega$, within which possible fracture is explicitly tracked along m failure paths (See Fig. 1). Let $\boldsymbol{\delta}^{(\alpha)}$ denote the spatially averaged separation (i.e., displacement jump) on the failure path, α ($\alpha = 1, 2 \ldots, m$). The macroscopic stress $\bar{\boldsymbol{\sigma}}(\mathbf{x}, t)$ at time t during the loading process is expressed as:

$$\bar{\boldsymbol{\sigma}}(\mathbf{x}, t) = \bar{\mathbf{L}} : \bar{\boldsymbol{\epsilon}}(\mathbf{x}, t) + \sum_{\alpha=1}^{m} \mathbf{Z}^{(\alpha)} \cdot \boldsymbol{\delta}^{(\alpha)}(\mathbf{x}, t) \tag{1}$$

where $\bar{\boldsymbol{\epsilon}}$ stands for macroscopic strain tensor; $\bar{\mathbf{L}}$ is the tensor of homogenized elastic moduli; $\mathbf{Z}^{(\alpha)}$ is a third order coefficient tensor that determines the stress contribution due to the separations on the failure path, α; $(\cdot)$ and $(:)$ respectively denote inner and double inner product operators. $\bar{\mathbf{L}}$ and $\mathbf{Z}^{(\alpha)}$ are computed as integrals of characteristic influence functions (i.e., numerical Green's functions) over the microstructure, and incorporate material heterogeneity and failure path morphology information. The coefficient tensors are evaluated by linear elastic analyses over the domain of the microstructure prior to the multiscale simulation. A brief introduction to the microstructure analysis is shown in the appendix.

The governing equilibrium equation within the microstructure is recast on each failure path as:

$$\mathbf{t}^{(\alpha)}(\mathbf{x}, t) - \mathbf{C}^{(\alpha)} : \bar{\boldsymbol{\epsilon}}(\mathbf{x}, t) + \sum_{\beta=1}^{m} \mathbf{D}^{(\alpha\beta)} \cdot \boldsymbol{\delta}^{(\beta)}(\mathbf{x}, t) = \mathbf{0} \tag{2}$$

where $\mathbf{t}^{(\alpha)}$ is the average traction vector on the failure path, α, and $\mathbf{C}^{(\alpha)}$ and $\mathbf{D}^{(\alpha\beta)}$ are coefficient tensors. The governing reduced order system of "mesoscale" equations is closed by introducing a traction-separation relationship to describe the cohesive behavior on the failure paths (expressed in a generic form):

$$\mathbf{t}^{(\alpha)} = \hat{\mathbf{t}}^{(\alpha)}\left(\boldsymbol{\delta}^{(\alpha)}, \mathbf{q}^{(\alpha)}\right) \tag{3}$$

where $\mathbf{q}$ denotes a vector of internal state variables that define the evolution of the cohesive law. In order to describe failure under the fatigue process, the cohesive law is taken to be cycle-sensitive and history-dependent. The MDDT framework admits various forms of constitutive laws for the cohesive behavior such as the classical bi-linear [36] and others (e.g. [26,27]). The specific evolution equations for the cohesive model employed in this study are discussed below.

2.2 Mesh-size objectivity

When unregularized and subjected to static or fatigue loading conditions, the MDDT model exhibits spurious mesh-size sensitivity and diminishing dissipated energy due to fracture as a function of increasing mesh density. The homogenization process results in a continuum description of damage at macroscale which is well known to result in spurious mesh-size sensitivity [31,32] in the presence of failure localization, despite the fact that failure is represented along discrete surfaces at the microscale. The issue of spurious mesh sensitivity is alleviated by enforcing overall fracture energy consistency [37]. Under static loading, leveraging the multiscale nature of the MDDT approach, the regularization effectively adjusts the size of the microstructure as a function of the characteristic macroscopic element size, so as to keep the macroscopic fracture energy independent of element size. The microstructure size adjustment is performed in an effective fashion by analytically expressing the corresponding reduced order model (i.e. coefficient tensors) as a function of macroscopic element size, rather than directly building and discretizing separate microstructures of different sizes for different macroscopic element sizes. The "reference" microstructure is the only one which is discretized for computing the coefficient tensors (i.e. reference coefficient tensors). The analytical relationship between the reduced order model and macroscopic element size has been established for cohesive laws that exhibit linear or near-linear softening behavior (e.g., bilinear law [36]) using the reference coefficient tensors. Let $\xi^{(\alpha)} = l/h^{(\alpha)}$ denote the length scale ratio, where l stands for the reference microstructure size (e.g., smallest RVE or unit cell) and $h^{(\alpha)}$ the characteristic length of the macroscale element along the direction dictated by the orientation of the failure path, α. The reduced order model associated with the length scale ratio, $\xi^{(\alpha)}$ is then obtained by scaling the reference coefficient tensors:

$$\hat{\mathbf{D}}^{(\alpha\beta)}\left(\xi^{(\alpha)}\right) = \boldsymbol{\eta}^{(\alpha)}\left(\xi^{(\alpha)}\right) \cdot \mathbf{D}^{(\alpha\beta)} \tag{4}$$

When expressed in terms of the local coordinate systems aligned with the unit normals and two tangential directions of the failure paths, the matrix form of the scaling tensor is diagonal:

$$\left[\boldsymbol{\eta}^{(\alpha)}\left(\xi^{(\alpha)}\right)\right] = \begin{bmatrix} \eta_N^{(\alpha)}(\xi^{(\alpha)}) & 0 & 0 \\ 0 & \eta_{S_1}^{(\alpha)}(\xi^{(\alpha)}) & 0 \\ 0 & 0 & \eta_{S_2}^{(\alpha)}(\xi^{(\alpha)}) \end{bmatrix} \tag{5}$$

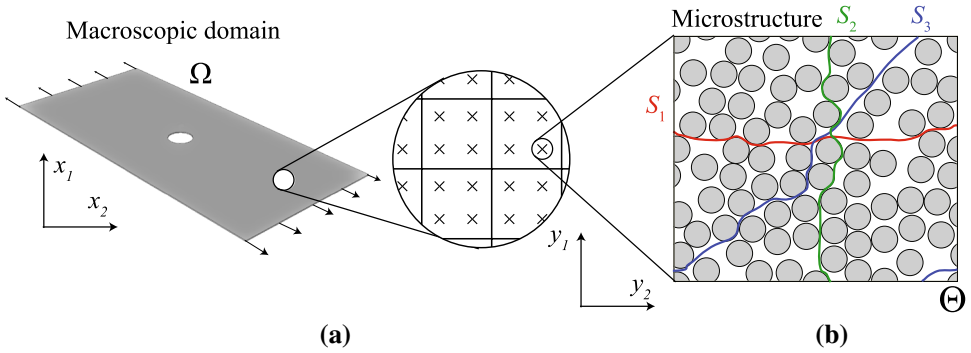

Fig. 1 Spatial multiscale modeling strategy for composite laminates. **a** Macroscopic domain **b** microstructure domain, S_i (i = 1,2,3) denote failure paths (surfaces in 3-D)

Scaled $\widetilde{\mathbf{Z}}^{(\alpha)}\left(\xi^{(\alpha)}\right)$ is defined in the matrix form as:

$$\left[\hat{\mathbf{Z}}^{(\alpha)}\left(\xi^{(\alpha)}\right)\right] = \begin{bmatrix} \eta_N^{(\alpha)}\mathbf{Z}_{11}^{(\alpha)} & \eta_{S_1}^{(\alpha)}\mathbf{Z}_{12}^{(\alpha)} & \eta_{S_2}^{(\alpha)}\mathbf{Z}_{13}^{(\alpha)} \\ \eta_{S_1}^{(\alpha)}\mathbf{Z}_{12}^{(\alpha)} & \mathbf{Z}_{22}^{(\alpha)} & \mathbf{Z}_{23}^{(\alpha)} \\ \eta_{S_2}^{(\alpha)}\mathbf{Z}_{13}^{(\alpha)} & \mathbf{Z}_{23}^{(\alpha)} & \mathbf{Z}_{33}^{(\alpha)} \end{bmatrix} \tag{6}$$

$\mathbf{D}^{(\alpha\beta)}$ and $\mathbf{Z}^{(\alpha)}$ are the reference coefficient tensors, taken as $\mathbf{D}^{(\alpha\beta)}\left(\xi^{(\alpha)}\right) = \hat{\mathbf{D}}^{(\alpha\beta)}\left(\xi^{(\alpha)} = 1\right)$ and $\mathbf{Z}^{(\alpha)} = \hat{\mathbf{Z}}^{(\alpha)}$ $(\xi^{(\alpha)} = 1)$, when the size of the reference microstructure equals the macroscopic element size. $\eta_N^{(\alpha)}, \eta_{S_1}^{(\alpha)}$ and $\eta_{S_2}^{(\alpha)}$ are respectively the scaling factors that are computed using coefficient tensor components in the normal and two orthogonal shear directions of the failure path:

$$\eta_N^{(\alpha)} = \frac{\xi^{(\alpha)} A_N^{(\alpha)}}{A_N^{(\alpha)} + \left(1-\xi^{(\alpha)}\right)\left(D_N^{(\alpha)}\bar{L}_N^{(\alpha)} + Z_N^{(\alpha)}C_N^{(\alpha)}\right)(\bar{L}_N^{(\alpha)})^{-1}} \tag{7}$$

$$\eta_{S_1}^{(\alpha)} = \frac{\xi^{(\alpha)} A_{S_1}^{(\alpha)}}{A_{S_1}^{(\alpha)} + \left(1-\xi^{(\alpha)}\right)\left(D_{S_1}^{(\alpha)}\bar{L}_{S_1}^{(\alpha)} + Z_{S_1}^{(\alpha)}C_{S_1}^{(\alpha)}\right)(\bar{L}_{S_1}^{(\alpha)})^{-1}} \tag{8}$$

$$\eta_{S_2}^{(\alpha)} = \frac{\xi^{(\alpha)} A_{S_2}^{(\alpha)}}{A_{S_2}^{(\alpha)} + \left(1-\xi^{(\alpha)}\right)\left(D_{S_2}^{(\alpha)}\bar{L}_{S_2}^{(\alpha)} + Z_{S_2}^{(\alpha)}C_{S_2}^{(\alpha)}\right)(\bar{L}_{S_2}^{(\alpha)})^{-1}} \tag{9}$$

where $A_N^{(\alpha)}$, $A_{S_1}^{(\alpha)}$ and $A_{S_2}^{(\alpha)}$ stand for the softening slopes of the traction-separation relationship, defined as $A_N^{(\alpha)} = \partial t_N^{(\alpha)}/\partial\delta_N^{(\alpha)}, A_{S_1}^{(\alpha)} = \partial t_{S_1}^{(\alpha)}/\partial\delta_{S_1}^{(\alpha)}, A_{S_2}^{(\alpha)} = \partial t_{S_2}^{(\alpha)}/\partial\delta_{S_2}^{(\alpha)}$. t_N, t_{S_1}, t_{S_2} and $\delta_N, \delta_{S_1}, \delta_{S_2}$ are respectively normal and two tangential components of the traction and separation vectors. $D_N^{(\alpha)}$, $D_{S_1}^{(\alpha)}, D_{S_2}^{(\alpha)}, C_N^{(\alpha)}, C_{S_1}^{(\alpha)}, C_{S_2}^{(\alpha)}, \bar{L}_N^{(\alpha)}, \bar{L}_{S_1}^{(\alpha)}, \bar{L}_{S_2}^{(\alpha)}$ are respectively linear compositions of the coefficient tensor components in terms of the aforementioned local coordinates of the failure path.

The regularization methodology is schematically illustrated in Fig. 2. Unlike the crack band approach [37], which also employs the strategy of energy consistency, the constitutive (i.e., traction-separation) behavior remains unchanged in the present approach. The microstructure size (i.e., the corresponding MDDT model) is adjusted instead to regularize dissipated energy within the microstructure. The softening slope of the resulting macroscopic stress-strain relationship varies as a function of the length scale parameter.

One consideration is the relationship between the size of the microstructure, physical observable within the localization band and the macroscopic mesh size. Let w and ρ, respectively denote the width of the localization band and the microcrack density within the band. l_0 denotes the size of the smallest microstructure that can represent the morphology (e.g., a single fiber unit cell in Fig. 2) with a single failure path, and $h = aw$ the size of the macroscopic element along the direction normal to the failure path. a is a constant that sets the macroscopic element size relative to localization band width w. Using the energy equivalence principle, the microcrack density within the localizing element must be set as: $\rho_h = \rho/a$. Noting that the microcrack density within the element is inversely proportional to the microstructure size, l, and defining $\rho_0 = 1/l_0$ as the crack density associated with the unit cell, we obtain:

$$\frac{l}{l_0} = \frac{\rho_0 h}{\rho w} \tag{10}$$

It follows from above that the size of the microstructure used in MDDT corresponds to the single fiber unit cell (i.e., $l = l_0$) if $h = \rho w l_0$.

The aforementioned regularization strategy has been demonstrated to be effective under static loading conditions [25], where fracture energy dissipation is dictated by the strain softening regime of the macroscopic element response. Generalization of this regularization strategy to fatigue requires additional considerations. Many constitutive laws (i.e., traction-separation) that idealize progressive degradation under cyclic loading dissipate substantial fraction of the fracture energy during the hardening stage of the loading process [7,17,26–29,32]. Some of the fatigue damage models do not employ a softening regime and idealize the entire degradation process during hardening [17,26–29]. Even in the absence of a softening stage, fatigue damage models exhibit mesh size sensitivity, albeit for a different reason. As a fracture process zone cannot form at the crack tip, crack tip stress becomes singular and damage growth accelerates with increasing mesh density [32]. The extension of the proposed regularization strategy to this class of cycle-sensitive

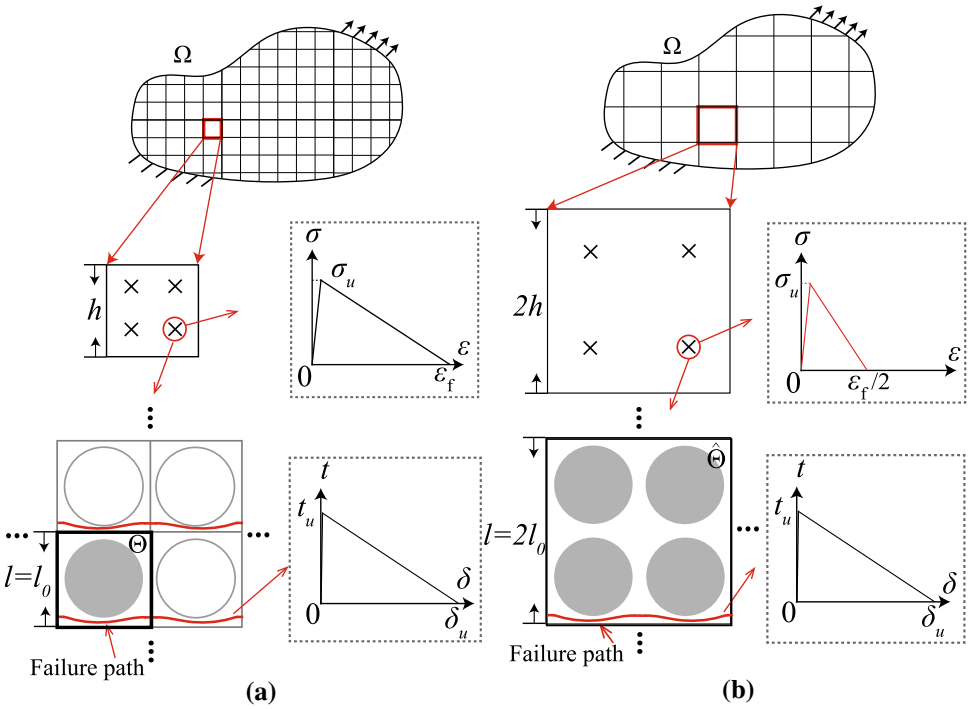

Fig. 2 Regularization strategy for mesh-size objectivity. **a** Macroscopic stress-strain relationship and cohesive behavior (i.e. traction-separation curve) when characteristic element size is h, **b** when characteristic element size is set to $2h$ using a larger microstructure

models is not straightforward. Instead, we adopt an alternative class of cycle-sensitive constitutive models, where the energy dissipation occurs during the softening stage [38].

2.3 Non-additive traction-separation law

This section provides the specific cohesive law used to idealize the progressive failure along a failure path subjected to cyclic loading. The proposed law is a variant of the constitutive model devised by Khoramishad et al. [38], who introduce two damage variables to describe the cycle-sensitive failure behavior. In what follows, superscript α that indicates the failure path index is omitted for simplicity of presentation. The traction-separation relationship is expressed as:

$$\mathbf{t} = (1-\omega)\mathbf{K}\cdot\boldsymbol{\delta} \tag{11}$$

where $\mathbf{K}$ represents the cohesive stiffness tensor, $[\mathbf{K}] = K\mathbf{I}$, and $\mathbf{I}$ is the second order identity tensor; $\omega \in [0,1]$ is a scalar damage variable. $\omega = 0$ denotes the initial state with full cohesive stiffness, $\omega = 1$ represents cohesionless crack along the failure path. Employing the classical bilinear form, the cohesive damage variable is expressed as:

$$\omega(\kappa) = \begin{cases} 0 & \kappa \le \nu_c \\ \dfrac{\nu_u\,(\kappa-\nu_c)}{\kappa\,(\nu_u-\nu_c)} & \nu_c < \kappa \le \nu_u \\ 1 & \kappa > \nu_u \end{cases} \tag{12}$$

where $\kappa(t) = \max_{\tau\in[0,t]}\{\nu(\tau)\}$ is the history variable of equivalent separation ν, $\nu = \|\boldsymbol{\delta}\| = \sqrt{\delta_N^2 + \delta_{S_1}^2 + \delta_{S_2}^2}$, where δ_N satisfies $\delta_N \ge 0$ to eliminate the possibility of interpenetration. ν_c and ν_u respectively correspond to the values of the equivalent separation at the onset of the softening region and at ultimate failure. They are evaluated under mixed-mode conditions based on a quadratic damage initiation criterion [36] and using the B-K criterion [39]:

$$\nu_c = \delta_{c_\mathrm{I}}^f \delta_{c_\mathrm{II}}^f \sqrt{\frac{1+{\beta_m}^2}{(\delta_{c_\mathrm{II}}^f)^2 + \left(\beta_m \delta_{c_\mathrm{I}}^f\right)^2}} \tag{13}$$

$$\nu_u = \frac{2}{K\nu_c}\left[G_{\mathrm{I}c}^f + (G_{\mathrm{II}c}^f - G_{\mathrm{I}c}^f)\left(\frac{{\beta_m}^2}{1+{\beta_m}^2}\right)^{\eta_{\mathrm{BK}}}\right] \tag{14}$$

where β_m is the mixed-mode ratio defined as the ratio between tangential and normal separations, $\beta_m = \sqrt{\delta_{S_1}^2 + \delta_{S_2}^2}/\delta_N$. Degradation behavior under repetitive cyclic loading is modeled by introducing the fatigue damage variable $\omega_f \in [0,1]$. Unlike ω, which degrades the instantaneous secant stiffness, the fatigue damage variable acts on the critical separation at the onset of damage and the critical energy release rate:

$$\delta_{c_\mathrm{I}}^f = \delta_{c_\mathrm{I}}\left(1-\omega_f\right), \quad \delta_{c_\mathrm{II}}^f = \delta_{c_\mathrm{II}}\left(1-\omega_f\right) \tag{15}$$

$$G_{\mathrm{I}c}^f = G_{\mathrm{I}c}(1-\omega_f)^2, \quad G_{\mathrm{II}c}^f = G_{\mathrm{II}c}(1-\omega_f)^2 \tag{16}$$

where, $\delta_{c_{\mathrm{I}}}$, $\delta_{c_{\mathrm{II}}}$ are equivalent separations at the onset of the softening region, $G_{\mathrm{I}c}$ and $G_{\mathrm{II}c}$ are critical fracture energies under mode-I and mode-II conditions. Under pure mode I loading ($\beta_m = 0$), the critical and ultimate equivalent separations become $\nu_c = \delta^f_{c_{\mathrm{I}}}$ and $\nu_u = \delta^f_{u_{\mathrm{I}}}$, respectively. Similarly, pure mode II loading ($\beta_m = \infty$) results in critical and ultimate equivalent separations of $\nu_c = \delta^f_{c_{\mathrm{II}}}$ and $\nu_u = \delta^f_{u_{\mathrm{II}}}$, respectively. $\delta^f_{c_{\mathrm{I}}}$, $\delta^f_{c_{\mathrm{II}}}$, $G^f_{\mathrm{I}c}$ and $G^f_{\mathrm{II}c}$ are effectively the fracture parameters of a cohesive interface that has been cyclically damaged by ω_f. Considering the bilinear form of the cohesive law: $t_u = K\delta_c$, $G_c = t_u\delta_u/2$, the fatigue degradation can also be regarded as reducing the peak traction t_u and ultimate equivalent separation δ_u: $t^f_u = t_u\left(1-\omega_f\right)$, $\delta^f_u = \delta_u\left(1-\omega_f\right)$. The stiffness and softening slope of the traction-separation relationship is not influenced by fatigue damage.

In order to account for the presence of fatigue damage variable, the history variable κ is expressed as:

$$\kappa(t) = \max_{\tau\in[0,t]}\left\{\frac{\nu(\tau)}{1-\omega_f(\tau)}\right\}\left(1-\omega_f(t)\right) \tag{17}$$

In the absence of cyclic degradation (i.e., $\omega_f = 0$), Eq. 17 degrades to its original definition.

With respect to the evolution law for fatigue damage, this work adopts separation-based form [32]:

$$\dot{\omega_f} = C\exp\left(\lambda\omega_f\right)\left(\frac{\nu}{\nu_u}\right)^{\beta_f}\frac{\langle\dot{\nu}\rangle_+}{\nu_u} \tag{18}$$

where λ is a material parameter, and $\langle\cdot\rangle_+ = [|\cdot| + (\cdot)]/2$ denotes the Macaulay brackets. In order to model fatigue damage evolution under mixed-mode conditions, the amplitude coefficient C and the power index β_f are respectively defined as functions of the mixed mode ratio (following the form of the B-K model [40]):

$$\ln C = \ln C_{\mathrm{II}} + [\ln C_{\mathrm{I}} - \ln C_{\mathrm{II}}](\frac{1}{1+\beta_m^2})^{m_c} \tag{19}$$

$$\beta_f = \beta_{f_{\mathrm{I}}} + (\beta_{f_{\mathrm{II}}} - \beta_{f_{\mathrm{I}}})(\frac{\beta_m^2}{1+\beta_m^2})^{m_{\beta_f}} \tag{20}$$

where $C = C_{\mathrm{I}}$, $\beta_f = \beta_{f_{\mathrm{I}}}$ indicate the material properties that control the fatigue damage evolution under pure mode I loading (i.e. $\beta_m = 0$), and $C = C_{\mathrm{II}}$, $\beta_f = \beta_{f_{\mathrm{II}}}$ under pure mode II (i.e., $\beta_m \to \infty$). Power indices m_c and m_{β_f} are additional parameters controlling damage evolution under mixed mode loading.

Figure 3 schematically illustrates a typical behavior of the cohesive law subjected to cyclic loading. For generality of demonstration, a separation-controlled variable amplitude loading is employed to generate the traction-separation curve. The figure illustrates that if the peak traction magnitude does not reach the instantaneous ultimate traction (i.e., t^f_u), the behavior is non-dissipative and t^f_u reduces under cyclic loading. The softening slope remains constant regardless of the value of t^f_u. The energy dissipation occurs only during the softening regime. This is crucial to regularization of MDDT model as it adjusts dissipated energy by regularizing the softening moduli of the homogenized stress-strain relationship.

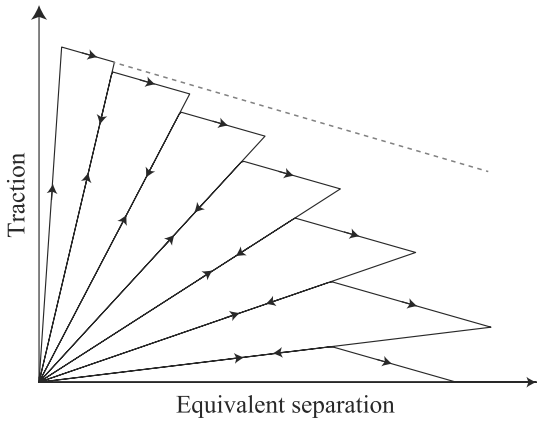

Fig. 3 Traction-separation curve obtained by non-additive scheme under cyclic loading. Dash line represents the bilinear profile obtained under monotonic loading

2.4 Temporal multiscale scheme

Straightforward time integration of the governing equations of the MDDT model to characterize long-term damage evolution and failure is computationally prohibitive for high cycle fatigue. In such a *cycle-by-cycle* approach, each loading cycle is discretized into several increments and the governing equations of the MDDT model is evaluated using a nonlinear solver (e.g., Newton-Raphson or others) for each increment of each cycle. Instead, we accelerate the simulations by adopting the multiple time scale life prediction methodology proposed in Ref. [26]. In this regard, we define two problems separated by the time scales they operate. The *microchronological* problem evaluates the response subjected to a single load cycle (summarized in Box A in the appendix). The *macrochronological* problem provides the long-term evolution of damage and equilibrium state. The governing system of equations are summarized in the appendix for brevity of this discussion.

The implementation of the multiple time scale approach is similar to the block-cycle modeling [18] and illustrated in Fig. 4. The micro- and macrochronological problems are evaluated in a tightly coupled fashion. At each macrochronological increment, t_i, a microchronological problem is evaluated to compute the rate of fatigue damage evolu-

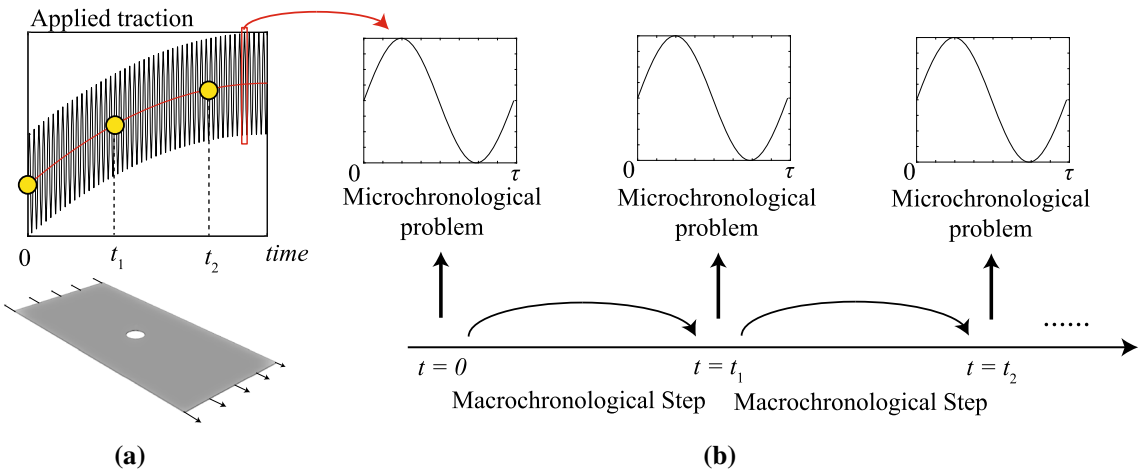

Fig. 4 **a** Fatigue loading history, **b** time domain decomposition in the temporal multiscale scheme

tion. The macrochronological time increments are adaptively set [27] based on maximum allowable damage accumulation ($\Delta\omega_p$) within a single increment.

Following Ref. [27], the microchronological problem is evaluated in a quasi-linear fashion, where the damage accumulation is assumed to not affect the equilibrium state within a single load cycle. By this approach, fatigue damage accumulation within the microchoronologcal problem is expressed in cyclic form as:

$$\frac{\mathrm{d}\omega_f}{\mathrm{d}N} = \frac{C(1-\omega_f)^{1+\beta_f}}{1+\beta_f}\exp\left(\lambda\omega_f\right)\left[\left(\frac{\nu_{max}}{\nu_u}\right)^{\beta_f+1} - \left(\frac{\nu_{min}}{\nu_u}\right)^{\beta_f+1}\right] \tag{21}$$

where ν_{max} and ν_{min} are respectively maximum and minimum equivalent separation within the unit loading cycle. Load characteristic such as the R-ratio natually affects fatigue damage accumulation in the microchronological problem. This is evident in Eq. 21 due to the presence of ν_{max} and ν_{min} terms.

The implementation of the MDDT modeling framework consists of the construction of the reduced order model that corresponds to the reference microstructure, and evaluation of the macroscopic, multichronological problem. The reference reduced order model is computed using an in-house code. The macroscopic problem is evaluated using the commercial finite element analysis package, ABAQUS. The reduced-order MDDT model as well as regularization scheme are incorporated using the user supplied subroutine capability, UMAT. The coupling between the micro- and macrochronological problems is implemented using Python scripts that involves the appropriate problem in turn as shown in Fig. 4.

3 Numerical verification

In this section, fatigue simulations using un-notched and open-hole laminate configurations are performed to verify the MDDT models in terms of (1) mesh-size objectivity and (2) capabilities in capturing complex failure mechanisms.

Figure 5 displays the configuration and discretization of the reference microstructure employed for all numerical examples in this study. The microstructure is a unit cell composed of square-packed unidirectional fiber reinforcement embedded in a continuous matrix. The elastic properties of isotropic matrix and transversely isotropic fiber constituents are listed in Table 1. The unit cell is 65% fiber by volume. Three potential failure paths that correspond to the primary failure modes of transverse matrix cracking, delamination and fiber fracture are considered, and reside within the domain of the respective constituents. As the intralaminar and interlaminar damage of matrix constituents are separately modeled in different domains of the numerical specimens, they are represented using two separate microstructures. The transverse matrix cracking and delamination failure paths have the same morphology and fracture properties, but they are oriented differently with respect to the ply lay up. In case of loading along the fiber direction, ultimate failure would constitute fracture in both fiber and matrix. In this study, fatigue fracture of the matrix ligament is ignored due to the significant moduli disparity between the fiber and the matrix, and the fiber fracture path is considered within the fiber domain only.

3.1 Unnotched specimen

The unnotched numerical specimens subjected to cyclic loading are employed for verification of the MDDT model. Figure 6 displays the geometry, loading and a sample dis-

Table 1 Elastic properties of matrix$^{(m)}$ and fiber$^{(f)}$

$E^{(m)}$ [GPa]	$\nu^{(m)}$	$E_1^{(f)}$ [GPa]	$E_2^{(f)}$ [GPa]	$G_{12}^{(f)}$[GPa]	$\nu_{12}^{(f)}$	$\nu_{23}^{(f)}$
3.55	0.35	263	13	27.5	0.32	0.20

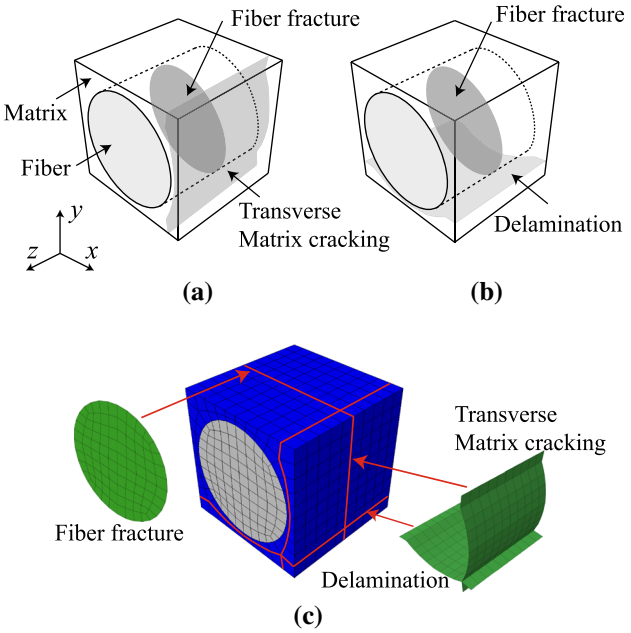

Fig. 5 Reference microstructure embedded with the failure paths of **a** transverse matrix cracking and fiber fracture, and **b** delamination and fiber fracture. **c** Discretizations of the reference microstructure and failure paths

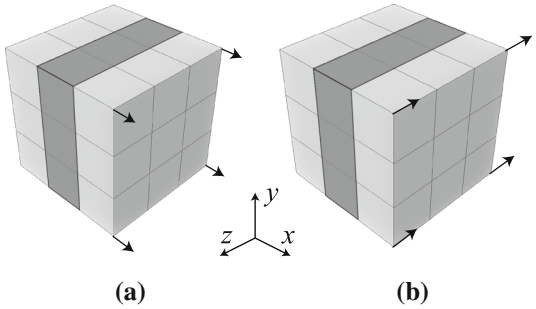

Fig. 6 Macroscopic domain of microscopic 90° unnotched specimen under **a** tensile loading, **b** shear loading

Table 2 Fracture parameters of matrix cracking for unnotched configuration

Cohesive Failure					
$G_{Ic}^{(m)}$ [MPa mm]	$G_{IIc}^{(m)}$ [MPa mm]	$t_{\text{uI}}^{(m)}$ [MPa]	$t_{\text{uII}}^{(m)}$ [MPa]	$K^{(m)}$ [MPa mm^{-1}]	$\eta^{(m)}$
0.03	0.045	60	90	6×10^7	1
Fatigue damage evolution					
$C_{\text{I}}^{(m)}$	$C_{\text{II}}^{(m)}$	$\beta_{f_{\text{I}}}^{(m)}$	$\beta_{f_{\text{II}}}^{(m)}$	$m_c^{(m)}, m_{\beta_f}^{(m)}$	$\lambda^{(m)}$
2×10^{-3}	1×10^{-3}	0.1	0.1	1	0.1

cretization of the specimens. The 90° unnotched numerical specimens are loaded under strain-controlled uni-axial tension and simple shear loading that respectively activate mode-I and mode-II dominant fracture in the matrix. The numerical specimens are chosen as microscopic in order to observe a non-brittle failure under cyclic tensile loading, which allows us to clearly demonstrate mesh-size objectivity. The MDDT model shown in Fig. 5a is therefore employed. The loading conditions considered do not activate fatigue fracture in the fiber. The fracture parameters for the transverse matrix cracking failure path is listed in Table 2. Compared to generic unidirectional carbon fiber reinforced thermoset composites, this example employs low mode-I and mode-II cohesive fracture energy release rates for the purposes of demonstration. More realistic material parameters are used in laminate analyses discussed in the next section. The loading amplitudes for uniaxial and simple shear loadings are respectively 1.02% and 2.5% total applied strain with R-ratio equals to 0 in both cases. In the uniaxial tension case, symmetry boundary conditions are applied at the three sides normal to x, y and z directions, respectively. In the shear case, the lateral side that is parallel to the failure path is fixed to ensure that the onset of mode-I failure is suppressed.

The macroscopic domain is discretized with different mesh densities, where the corresponding length scale ratio is set to be $\xi = 1, 2, 4, 8, 16$ for verification of mesh-size objectivity. In the simple shear case, the coarsest discretization ($\xi = 1$) does not adequately resolve shear deformation and is not used. Damage localization is generated by disturbing the properties of one layer of elements lying parallel to the matrix failure path. 8-noded tri-linear hexahedral elements with reduced integration and hourglass control are employed in the macroscale discretizations. Simulations using the temporal multiscale integration scheme as well as the reference direct cycle-by-cycle time integration are performed. In the reference simulations, the vast majority of the increments resolve the non-linear response in the loading or reloading regime. The fatigue damage tolerance parameter that adaptively controls macrochronological time step size is set to be 1% or 2% in the simulations that use the temporal multiscale scheme.

Figure 7a, b show the predicted fatigue life for different mesh sizes under tensile and shear loading conditions, respectively. In this example, fatigue life refers to the number of load cycles, where the load carrying capacity of the structure vanishes (i.e., damage in the matrix crack failure path,

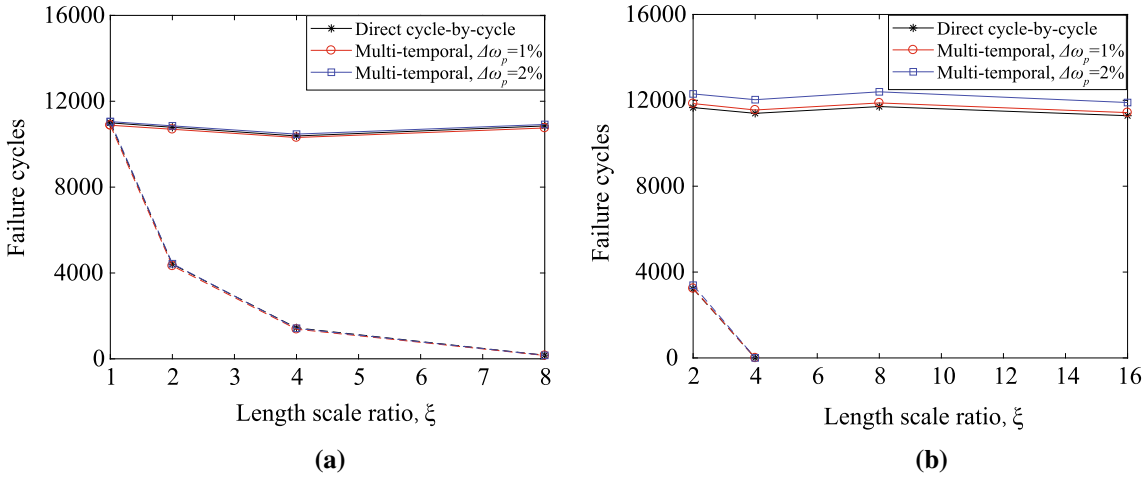

Fig. 7 Fatigue life versus length scale ratio (i.e. $\xi = l/h$) obtained by direct cycle-by-cycle scheme and temporal multiscale scheme with 1% and 2% tolerance for adaptive macrochronological time stepping strategy under **a** uniaxial and **b** shear loading. Solid lines show results with regularization, while dash lines indicate unregularized model

$\omega^{(m)} = 1$). The solid curves indicate predicted fatigue life when the regularization approach is employed, whereas the dash curves are the results of the unregularized simulations. In all cases, the temporal multiscale scheme exhibits good agreement with the direct cycle-by-cycle scheme. The corresponding average errors with step adaptivity tolerances of 1% and 2% are respectively less than 1.5% and 6% for all mesh size discretizations in both uniaxial and shear loaded cases. In contrast, the computational cost of the multiscale time integration scheme is significantly less than the reference scheme. The temporal multiscale scheme requires a total of 90 (normal) and 75 (shear) resolved cycles on average for tolerance of 1%, and 46 (normal) and 39 (shear) resolved cycles on average for tolerance of 2%, compared to 10,753 (normal) and 11,512 (shear) cycles resolved in the direct cycle-by-cycle scheme. A tradeoff exists between prediction accuracy and computational efficiency when choosing the tolerance: smaller value leads to higher accuracy but requires more macro-chronological time steps that reduces the efficiency of the approach. Because 2% tolerance has higher computational efficiency and also keeps reasonable accuracy, the open-hole simulations performed in this manuscript employ the temporal multiscale time integration algorithm with 2% tolerance.

Figure 8 displays stiffness evolution of the specimen as a function of load cycles when the tolerance is taken to be 1%. In terms of both fatigue life (Fig. 7) and stiffness loss, the MDDT model yields mesh-size consistent fatigue behavior with regularization (represented by solid lines). On the contrary, the non-regularized MDDT model (represented by dash lines) accelerates stiffness loss and leads to shortened fatigue life when element size is reduced. In the case of shear loaded unnotched specimen, mesh size sensitivity is so severe that fine resolution simulations show immediate failure within the first cycle.

3.2 Analysis of open-hole unidirectional specimens

In this section, the capabilities of the MDDT model are demonstrated in predicting stable crack growth under fatigue loading conditions in a mesh size objective manner. The analysis is performed in the context of an open-hole 0° unidirectional tape. Figure 9 illustrates the geometry, loading and boundary conditions, and discretizations used in this study. The overall width, length and thickness of the specimen are 20mm, 28mm and 0.125mm, respectively. The hole radius is 3.175mm. 1/8 of the specimen is discretized with symmetry boundary conditions applied at the three directions, leveraging symmetries of the specimen. As shown in Fig. 9b, the parts of the specimen, where the potential crack propagation is expected, is discretized with elements aligned with fiber direction to eliminate mesh bias effect. Different mesh sizes of 0.1mm, 0.05mm, 0.025mm, 0.0125mm within the potential crack propagation region of the specimen were used in order to verify mesh-size consistency. In the thickness direction, the ply is discretized using one element.

Table 3 lists the fracture properties for both failure paths of transverse matrix cracking and fiber fracture, which are consistent with generic unidirectionally carbon fiber reinforced thermoset composites. The parameters for fatigue damage evolution are selected within a reasonable range that the corresponding crack propagation rate is of the same order as experiments described in Ref. [9]. The analysis presented herein is focused on verification of mesh size objectivity. A formal calibration/validation study of a particular composite

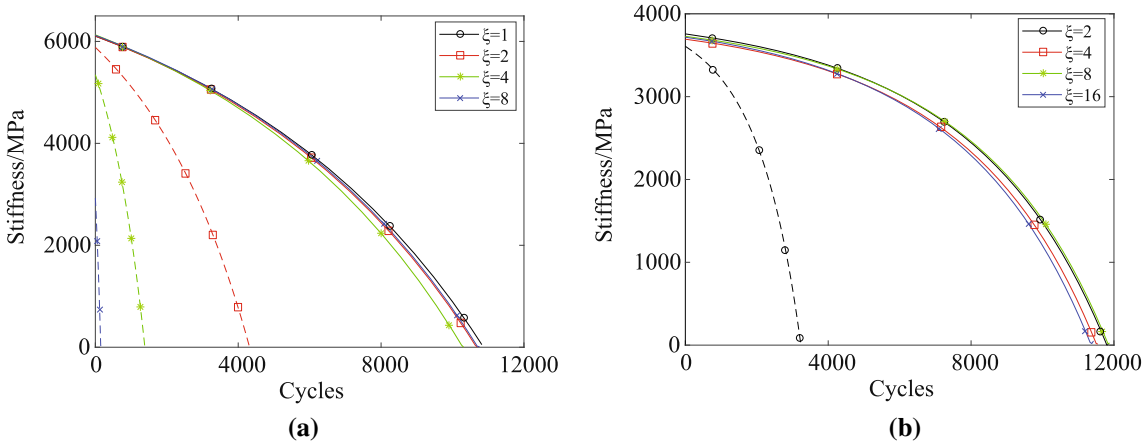

Fig. 8 Residual stiffness versus cycles obtained by the temporal multiscale scheme with 1% tolerance under **a** uniaxial and **b** shear loading. Solid lines show the results with regularization, while dash lines indicate the unregularized model

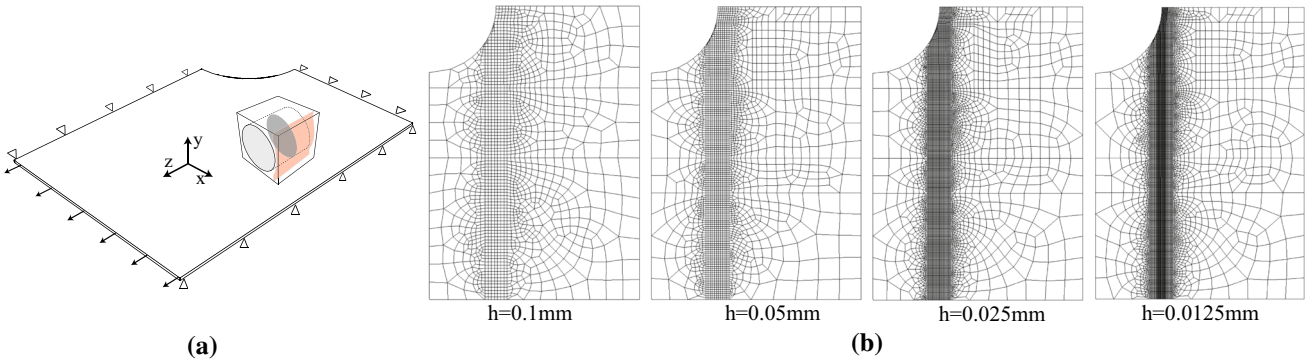

Fig. 9 **a** Geometry, boundary and loading conditions, and the MDDT model configuration for open-hole 0° ply single lamina analysis. **b** Different mesh discretizations using the size of h = 0.1 mm, 0.05 mm, 0.025 mm, 0.0125 mm

(See [26,28]) is outside the scope of the current manuscript, and will be the emphasis of future studies.

Force-controlled uniaxial cyclic loading with an amplitude of 482 MPa (80% of static strength) is applied to the specimen along z-direction with R-ratio equal to 0. The temporal multiscale scheme with 2% fatigue-damage tolerance for adaptive macro-chronological time stepping strategy is employed for the open-hole configurations.

Figure 10 shows the contours of shear stress σ_{xz} captured at the first cycle, 30,000 cycles and 300,000 cycles which are predicted using the regularized MDDT model. The macroscopic crack is displayed by light colored elements (shown as red in the electronic version of the manuscript) which have reached completed damage state ($\omega^{(m)} = 1$). A single dominant splitting crack initiates at the hole brim at the first cycle and grows aligned with the fiber (vertical) direction under subsequent cyclic loading. No fiber damage is observed in this case. The fracture process zone ($0 < \omega^{(m)} < 1$) is represented by the white straight line ahead of the splitting crack and results in low shear stress around 90 MPa as splitting crack is mode-II dominant. The length of the fracture process zone becomes shorter with increasing crack length, because the stress concentration at the crack tip reduces as the split grows. The patterns of crack propagation and fracture process zone are both mesh-size consistent. Figure 11 displays the cyclic evolution of crack propagation and stiffness as a function of load cycles. Without regularization, the splitting crack propagation and stiffness loss drastically accelerates with decreasing macroscopic element size. For the regularized MDDT model, the initial crack growth occurs faster compared to the non-regularized cases. This is because, the regularized MDDT model is referenced to the case with the element size (i.e. damage localization width) of $h = l = 0.01$mm, which is significantly finer than the finest mesh employed in this study. In addition, the results of the regularized MDDT model exhibits mesh-size consistent crack propagation rates and stiffness evolution. The crack growth and stiffness evolution curves also demonstrate converging trends with higher mesh densities. This indicates that the discrepancy between the regularized curves can be largely attributed to mesh resolution effects rather than spurious mesh size sensitivity.

Table 3 Fracture parameters for open-hole configuration

Cohesive failure for matrix cracking					
$G_{Ic}^{(m)}$ [MPa mm]	$G_{IIc}^{(m)}$ [MPa mm]	$t_{\mathrm{uI}}^{(m)}$ [MPa]	$t_{\mathrm{uII}}^{(m)}$ [MPa]	$K^{(m)}$ [MPa mm^{-1}]	$\eta^{(m)}$
0.2	1	60	90	6×10^7	1

Fatigue damage evolution for matrix cracking and delamination					
$C_{\mathrm{I}}^{(m)}$	$C_{\mathrm{II}}^{(m)}$	$\beta_{f_{\mathrm{I}}}^{(m)}$	$\beta_{f_{\mathrm{II}}}^{(m)}$	$m_c^{(m)}, m_{\beta_f}^{(m)}$	$\lambda^{(m)}$
1×10^{-2}	1×10^{-4}	0.1	0.1	1	0.1

Cohesive failure & fatigue damage evolution for fiber fracture							
$G_{\mathrm{Ic}}^{(f)}, G_{\mathrm{IIc}}^{(f)}$ [MPa mm]	$t_{\mathrm{uI}}^{(f)}, t_{\mathrm{uII}}^{(f)}$ [MPa]	$K^{(f)}$ [MPa mm^{-1}]	$\eta^{(f)}$	$C_{\mathrm{I}}^{(f)}, C_{\mathrm{II}}^{(f)}$	$\beta_{f_{\mathrm{I}}}^{(f)}, \beta_{f_{\mathrm{II}}}^{(f)}$	$m_c^{(f)}, m_{\beta_f}^{(f)}$	$\lambda^{(f)}$
12	4000	4×10^9	1	10^{-7}	0.1	1	0.1

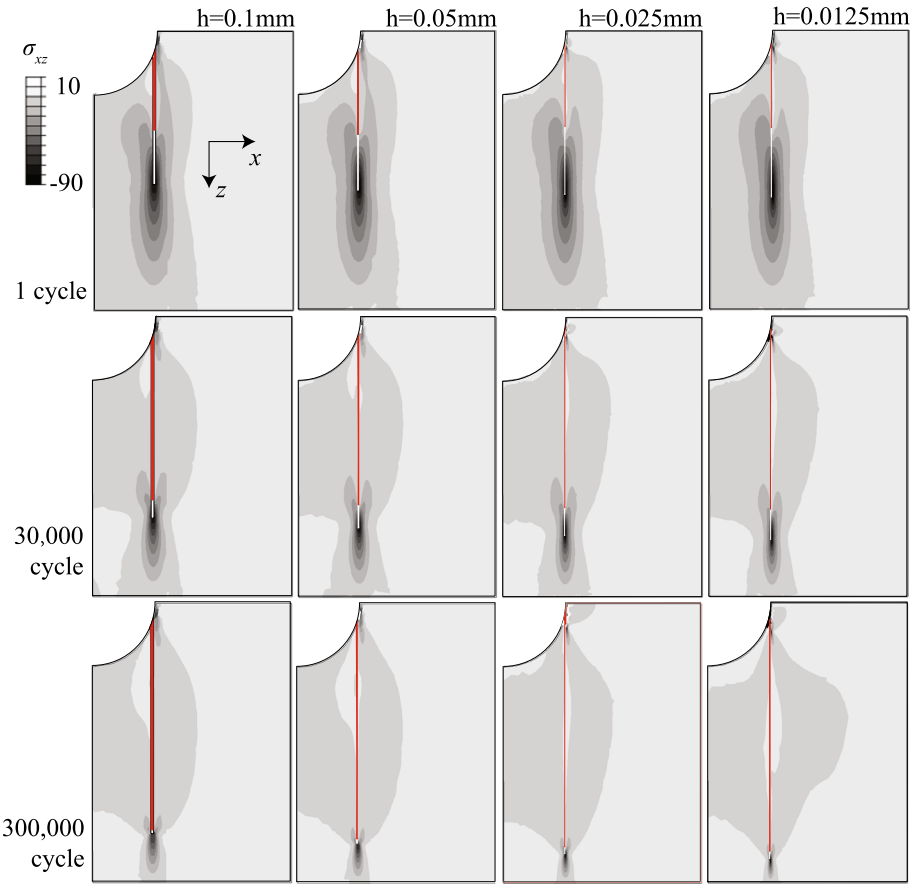

Fig. 10 Shear stress contour σ_{xz} captured at the first cycle, 3×10^4 cycles and 3×10^5 cycles for 0° ply single lamina with mesh densities of h = 0.1 mm, 0.05 mm, 0.025 mm, 0.0125 mm

3.3 Analysis of cross-ply open-hole specimens

The capabilities of the proposed multiscale model are further assessed in a composite specimen configuration that exhibits diffuse damage, cracking and multiple failure mechanisms. We consider an open-hole $[90°/0°]_S$ cross-ply laminate configuration subjected to tensile fatigue loading. Figure 12 illustrates the geometry, loading and boundary conditions, and discretizations used in this case. Similar to the previous example, 1/8 of the specimen is modeled leveraging the symmetries in the laminate and geometry. Model parameters shown in Tables 1 and 3 are employed. Force-controlled uniaxial cyclic loading of 313 MPa (90% of static strength) is applied to the specimen along the z-direction with R-ratio equal to 0. Previous experimental observations reveal the presence of delamination that affects fatigue damage progression in carbon-fiber reinforced thermoset resins [9,41,42]. In order to better capture the kinematics of delamination prop-

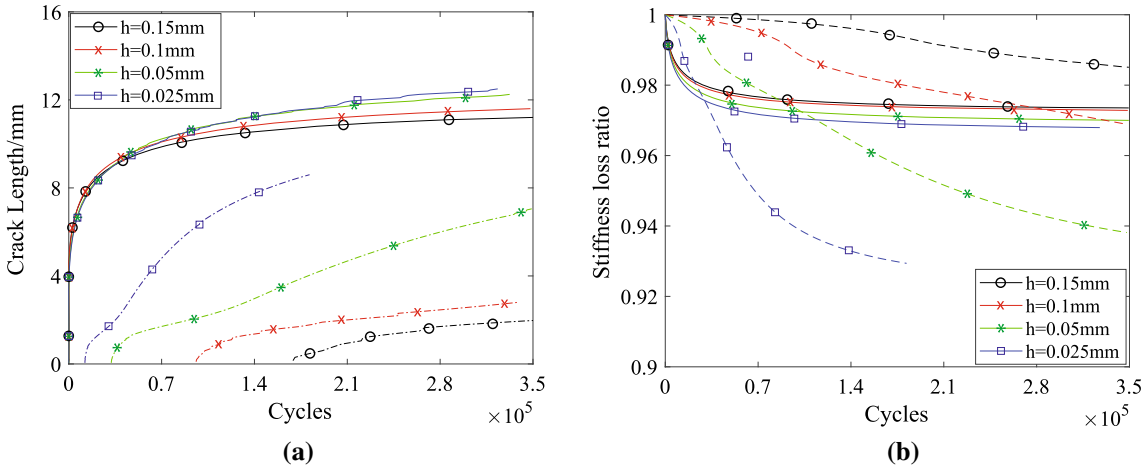

Fig. 11 **a** Splitting crack extension and **b** residual stiffness loss ratio as a function of cycle number for 0° lamina. Solid and dash lines respectively denote the results obtained by regularized and non-regularized models

agation, delamination is modeled by inserting an additional thin layer of macroscopic elements in between the 90° and 0° plies, in which the associated microstructure is embedded with delamination failure path, shown in Fig. 5b. The microstructure employed for delamination layer elements is identical to the ply layers, except for the difference of failure path orientations between delamination and transeverse matrix crack (See Fig. 5a,b). The thickness of the delamination layer is set to be 10 microns (8% ply thickness). MDDT regularization procedure ensures that the fracture energy consistency is satisfied regardless of the thickness of the delamination layer. The potential crack propagation region is discretized using the element sizes of 0.15 mm, 0.1 mm, 0.05 mm in order to verify mesh-size objectivity (see Fig. 12b). As demonstrated in the simulations below, transverse matrix cracks within the 90° ply are bridged by fibers within 0° ply, and the damage does not fully localize. In the absence of damage localization, fracture energy associated with transverse matrix cracking in the 90° ply is mesh-size independent without the need for regularization. Applying regularization would result in an unphysical increase of fracture energy with mesh refinement, which suppresses this failure mode when fine meshes are used. In what follows, we therefore do not employ the regularization scheme for 90° transverse matrix cracks.

Figure 13 shows the damage contours for transverse matrix cracking in the 90° ply shown as dark region (black color in the electronic version), for splitting crack in the 0° ply shown as the light grey region (light blue color in the electronic version), and for delamination shown as medium grey (red color in the electronic version). Delamination contours are shown in both 90° and 0° plies. The figure shows the results using different mesh densities captured after the first load cycle, 160,000 cycles and 320,000 cycles. The first cycle of loading results in a substantial amount of damage near the hole that consist of a diffuse region of transverse matrix cracking in the 90° ply, a dominant split in the 0° ply with length in the order of the hole radius, and some delamination. The level of damage observed is expected as the loading amplitude is large (90% of the static strength of the specimen). While significant damage is observed at the end of the first load near the hole, none of the failure paths reach full fracture state within the specimen (i.e., corresponding damage variable reaching unity). Subsequent cycling results in stable growth of all three damage mechanisms. Distinct, yet diffuse transverse matrix cracks begin to grow in the 90° ply but arrested by the splitting crack. Delamination growth occurs around the growing split and the transverse cracks. A small amount of fiber damage also occurs near the hole (not shown in figure) and grows slowly compared with the matrix damage. The general feature of damage contours conform well with the X-ray tomography of the damage in the high cycle fatigue cases of Refs. [9,41,42], which employ similar laminate configurations. No significant difference in crack extension patterns appear when different meshes are used in the simulations.

Figure 14 shows the growth of the dominant splitting crack as a function of load cycles, as well as the evolution of specimen stiffness. Crack growth is considered to initiate when full damage in the "transverse matrix crack" failure path is reached in the first element along the split. The crack growth process follows a short incubation period. During the incubation period, damage growth does not fully localize (as shown in top rows of Fig. 13), and the regularization is not effective. This manifests itself in the differences in crack growth initiation cycles shown in Fig. 14a. The number of cycles during incubation are respectively 4577 cycles, 9911 cycles and 17,864 cycles for the simulations with coarse (h = 0.15 mm), medium (0.1 mm) and fine (0.05 mm) meshes. The cycles to initiation constitutes a small portion of the struc-

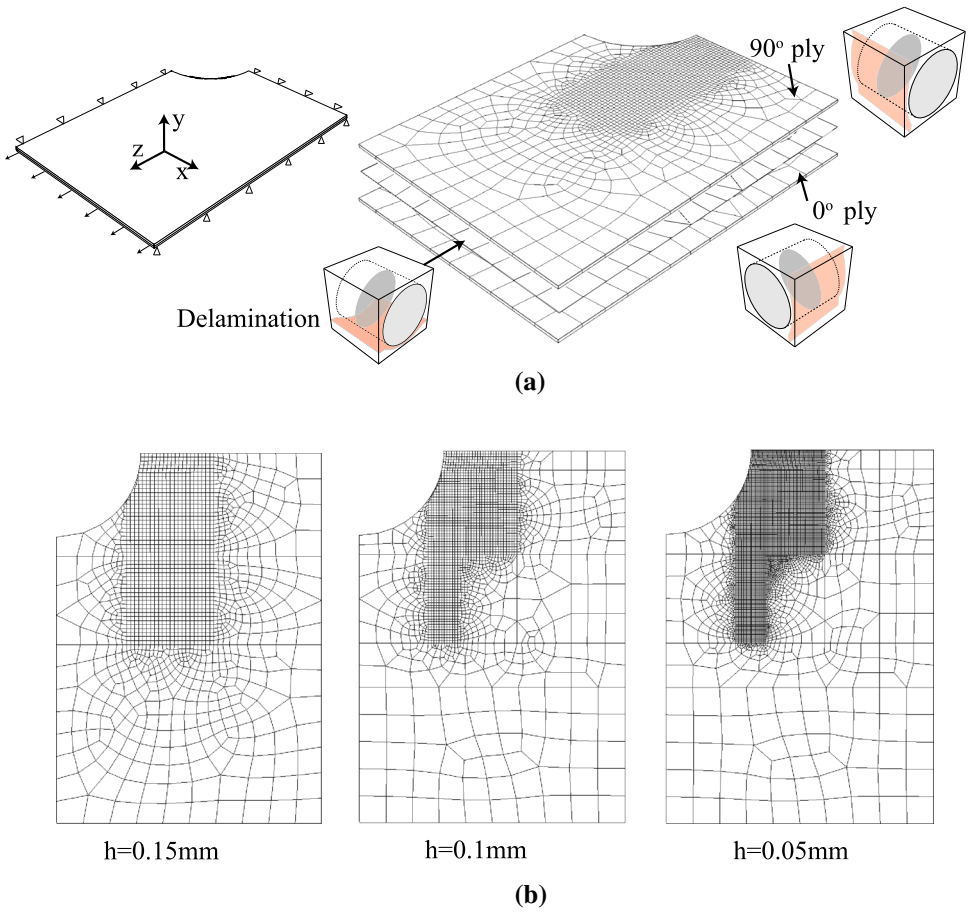

Fig. 12 **a** Geometry, boundary and loading conditions for the open-hole $[90°/0°]_S$ cross-ply laminates, as well as microstructure configuration for each ply and delamination modeling. **b** Different mesh densities with h = 0.15 mm, 0.05 mm, 0.025 mm for discretization

tural life and the errors do not affect the overall life prediction significantly. A reasonable overall mesh-size consistency is observed in both splitting crack growth and stiffness evolution curves.

We further conduct a parametric study on the relative fatigue sensitivity of mode-I and mode-II damage growth rates, and its consequences on specimen level damage evolution in the context of open-hole cross-ply laminate configurations. In this manuscript, the mode sensitivity is demonstrated by varying the fatigue amplitude parameters (i.e. $C_{\mathrm{I}}^{(m)}$ and $C_{\mathrm{II}}^{(m)}$), which affect the fatigue behavior, but not the static response. Other parameters such as the cohesive strength are expected to show similar influences. In this case, the amplitude parameter $C_{\mathrm{I}}^{(m)}$ that controls fatigue evolution (of "transverse matrix cracking" and "delamination" fatigue paths) under mode-I condition is reduced from 10^{-2} to 10^{-6}, while $C_{\mathrm{II}}^{(m)}$ and the rest of the parameters remain the same. This choice of the parameter effectively reduces the sensitivity of cyclic propagation of mode-I crack. The structural mesh is discretized with the element size of h = 0.1 mm. Figure 15 makes the comparison of predicted damage contours between $C_{\mathrm{I}}^{(m)} = 10^{-2}$ and $C_{\mathrm{I}}^{(m)} = 10^{-6}$ at 320,000 cycles. The splitting crack in the 0° ply, the interlaminar damage in the delamination layer, as well as the diffuse damage in 90° ply for $C_{\mathrm{I}}^{(m)} = 10^{-6}$ remain unchanged, but no discrete transverse cracks are observed. As shown in Fig. 16, the absence of transverse cracks does not have a significant influence on splitting crack extension, but reduces the stiffness loss steadily as the cyclic loading continues.

The differences in behavior is further illustrated by studying mode-I and mode-II fatigue damage evolution. Figure 17a compares the pure-mode fatigue damage evolution rate $\mathrm{d}\omega_f/\mathrm{d}t$ as a function of dimensionless equivalent separation v/v_u between $C_{\mathrm{I}}^{(m)} = 10^{-6}$ and $C_{\mathrm{I}}^{(m)} = 10^{-2}$. The figure plots Eqs. 18, 19, 20 with the respective material parameters. In the case of $C_I^{(m)} = 10^{-6}$, the pure mode-I fatigue degradation is orders of magnitude smaller than mode-II failure, whereas the opposite conclusion is reached for the case of $C_{\mathrm{I}}^{(m)} = 10^{-2}$. Noting that the transverse and the splitting cracks are respectively mode-I and mode-II dominated, setting $C_{\mathrm{I}}^{(m)} = 10^{-6}$ results in a much smaller transverse crack growth rate compared to the splitting crack. Conversely, setting $C_{\mathrm{I}}^{(m)} = 10^{-2}$ enhances transverse crack propagation and more interaction with the growing splitting crack

The two distinctly different behaviors have also been observed in experiments that use similar laminate configurations but different types of materials for matrix con-

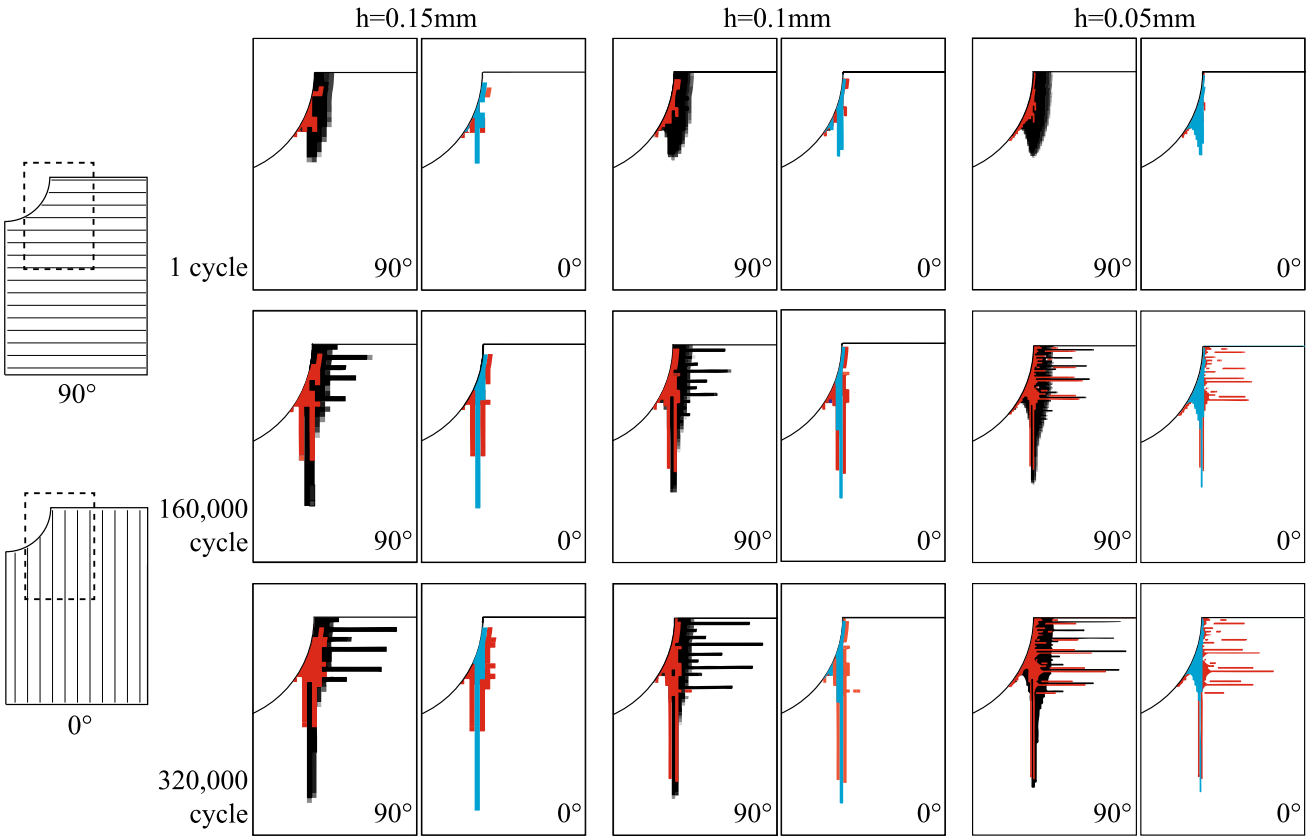

Fig. 13 Transverse matrix crackings (black) in 90°, splitting crack (light blue) in 0° ply, as well as delamination (red) captured at the first cycle, 160,000 cycles and 320,000 cycles for different mesh sizes of h = 0.15 mm, 0.1 mm, 0.05 mm. (Colour figure online)

stituents. According to the experiments conducted by Spearing et al. [41], T300/914C laminates subjected to high-fatigue cyclic loading shows long extension of transverse cracks, which are almost negligible in AS4/PEEK laminates observed by Wang et al. [43]. Figure 17b shows the typical fatigue crack growth rate curves for T300/914C and AS4/PEEK composite systems. The curves are generated by assuming that the fatigue crack propagation follows the Paris law with parameters calibrated using double cantilever beam and end notch flexure tests [44,45]. The switch between mode I and mode II fatigue sensitivity observed for the thermoset and thermoplastic systems and the experimentally observed damage propagation behavior are qualitatively in agreement with the trends shown in the parametric study.

4 Conclusion

This study proposed a new computational framework based on multiscale discrete damage theory (MDDT) for fatigue failure prediction of laminated composite structures. The MDDT model offers reduced-order homogenized representation of microscale fracture events along the discrete failure paths within which progressive fatigue loading induced failure occurs. Mesh-size objectivity is attained by adjusting microstructure size in an effective manner with respect to macroscopic element size. The MDDT model is integrated with temporal multiscale modeling and an adaptive time step selection strategy to achieve high computational efficiency. Our investigations indicate that energy regularization based on element size could be ineffective for fatigue damage accumulation unless specific forms of fatigue damage evolution laws are considered. In particular, fatigue damage laws (a) must include softening behavior (to eliminate stress state singularities at the crack tip) and (b) must dissipate fatigue fracture energy in the softening regime (for effective energy regularization). Numerical verification studies performed on open-hole laminate configurations subjected to high-fatigue tensile loading indicate the proposed multiscale model is mesh-size insensitive in terms of damage growth, crack propagation as well as specimen stiffness evolution. For cross-ply laminates, simultaneous growth of splitting, delamination and transverse matrix cracks, their distribution and growing patterns predicted by the proposed model agree well with experimental results. Furthermore, differences between the fatigue damage growth patterns observed in some thermoset and thermoplastic resins can be explained based on the rel-

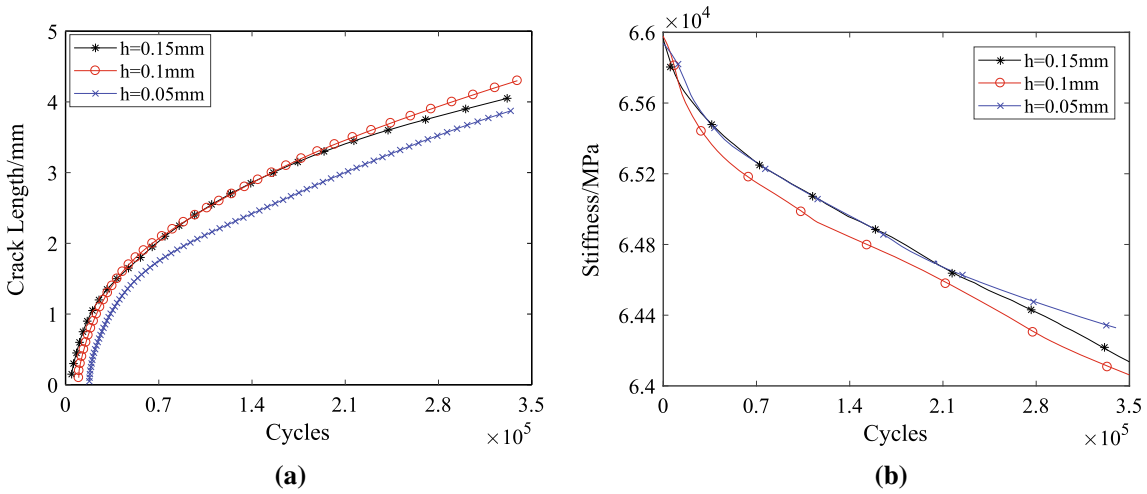

Fig. 14 **a** Splitting crack propagation, and **b** residual stiffness as a function of cycle numbers for $[90°/0°]_S$ laminates

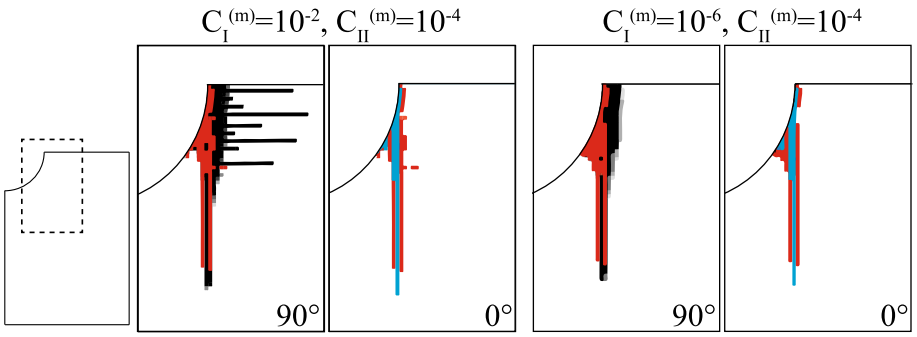

Fig. 15 Transverse matrix crackings (black) in 90°, splitting crack (light blue) in 0° ply and delamination (red) captured at 320,000 cycles compared between $C_{\mathrm{I}}^{(m)} = 0.01$, $C_{\mathrm{II}}^{(m)} = 10^{-4}$ and $C_{\mathrm{I}}^{(m)} = 10^{-6}$, $C_{\mathrm{II}}^{(m)} = 10^{-4}$. (Colour figure online)

ative fatigue resistances against mode I and mode II fatigue crack growth.

Acknowledgements The authors gratefully acknowledge the financial support of the Office of Naval Research Airframe Structures and Materials (Award No: N00014-17-1-2040, Program Manager: Dr. Anisur Rahman).

Appendix

Microstructure analysis

Consider the microstructure domain shown in Fig. 1, the displacement field $\mathbf{u}$ is expressed in terms of a two-scale asymptotic decomposition:

$$\mathbf{u}\left(\mathbf{x}, \mathbf{y}, t\right) = \mathbf{u}^0\left(\mathbf{x}, t\right) + \zeta \mathbf{u}^1\left(\mathbf{x}, \mathbf{y}, t\right) \tag{A.1}$$

where $\mathbf{u}^0$ is continuous and constant displacement field over the microstructure, ζ stands for scaling parameter between the two scales $\mathbf{y}(\mathbf{x}) = \mathbf{x}/\zeta$. The microscopic crack results in a displacement jump within the microstructural displacement field $\mathbf{u}^1 : \boldsymbol{\delta}\left(\mathbf{x}, \mathbf{y}, t\right) := [\![\mathbf{u}^1]\!]$. Both $\mathbf{u}^1$ and $\boldsymbol{\delta}$ are periodic along with the microstructure. Based on mathematical homgenization theory, the microstructural displacement field is expressed as:

$$\mathbf{u}^1\left(\mathbf{x}, \mathbf{y}, t\right) = \mathbf{H}\left(\mathbf{y}\right) : \boldsymbol{\epsilon}^0\left(\mathbf{x}, t\right) + \sum_{a=1}^{m} \left(\mathbf{h}_\alpha * \boldsymbol{\delta}_\alpha\right)\left(\mathbf{x}, \mathbf{y}, t\right) \tag{A.2}$$

where, $\boldsymbol{\epsilon}^0 = \nabla_{\mathbf{x}}^s \mathbf{u}^0$, $\nabla_{\mathbf{x}}^s$ is the symmetric gradient operator with respect to the macroscopic coordinates. $\mathbf{H}$ is the influence function that provides the variation of the elastic response over the microstructure volume without fracture. Another influence function $\mathbf{h}_\alpha$ is computed as responses to the separation of dirac function form d applied along the discontinuity path of failure path α ($\hat{\mathbf{y}} \in S_\alpha$): $[\![\mathbf{h}_\alpha(\mathbf{y}, \hat{\mathbf{y}})]\!] = \mathrm{d}(\mathbf{y} - \hat{\mathbf{y}})$.

Reduced-order approximation is employed for separation as a function of nonlocal weight functions $\nu^{(\alpha)}$ defined at failure path α to alleviate computational efforts of direct homogenization method:

$$\boldsymbol{\delta}^{(\alpha)}\left(\mathbf{x}, t\right) = \int_{S_\alpha} \nu^{(\alpha)}\left(\hat{\mathbf{y}}\right) \boldsymbol{\delta}\left(\mathbf{x}, \hat{\mathbf{y}}, t\right) d\hat{\mathbf{y}} \tag{A.3}$$

Premultiplying the microscale equilibrium equation $\nabla_{\mathbf{y}} \cdot \boldsymbol{\sigma}\left(\mathbf{x}, \mathbf{y}, t\right) = \mathbf{0}$ by influence function $\mathbf{h}_\alpha$, integrating over the

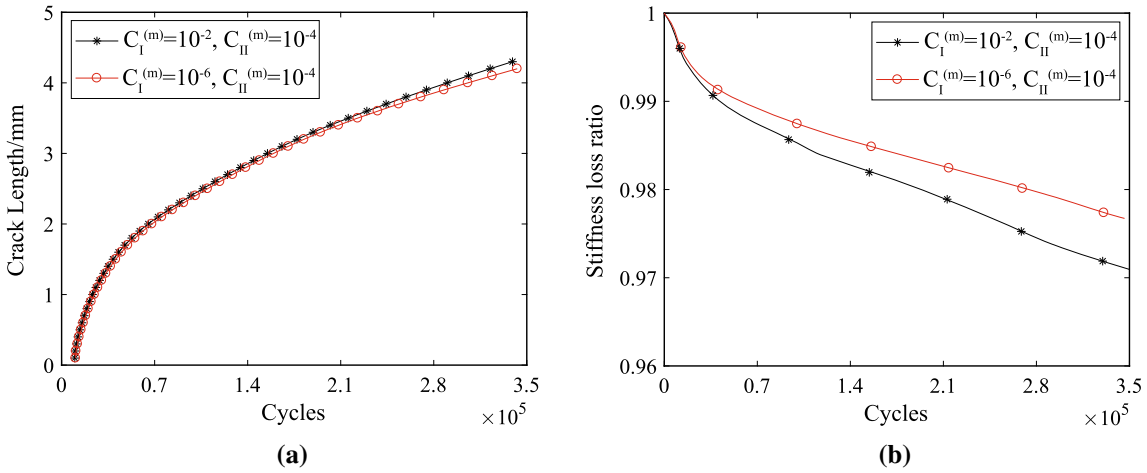

Fig. 16 **a** Splitting crack propagation, and **b** residual stiffness as a function of cycle numbers for $[90°/0°]_S$ laminates compared between $C_{\mathrm{I}}^{(m)} = 0.01$, $C_{\mathrm{II}}^{(m)} = 10^{-4}$ and $C_{\mathrm{I}}^{(m)} = 10^{-6}$, $C_{\mathrm{II}}^{(m)} = 10^{-4}$

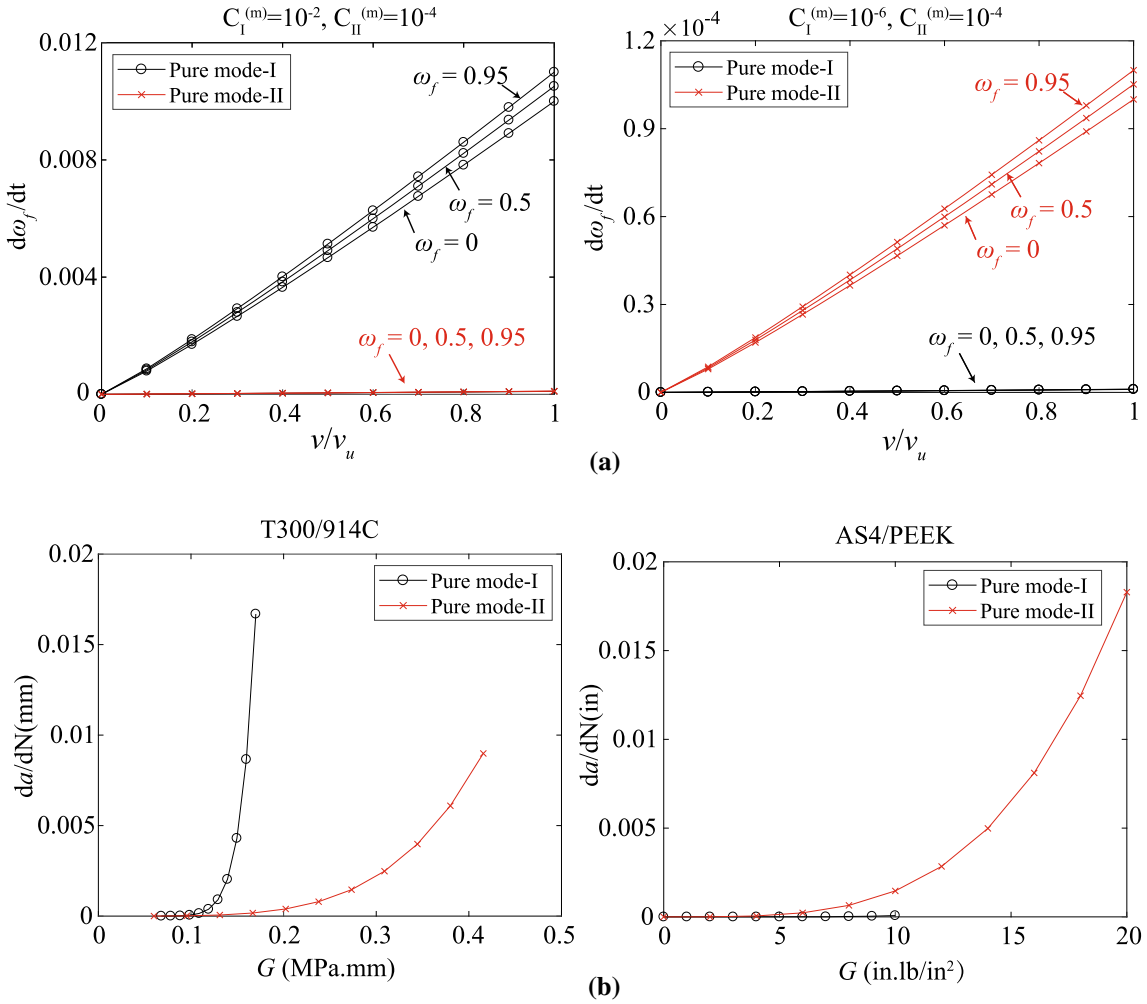

Fig. 17 **a** Pure mode fatigue damage evolution rate $\mathrm{d}\omega_f/\mathrm{d}t$ versus dimensionless equivalent separation v/v_u for $C_{\mathrm{I}}^{(m)} = 0.01$, $C_{\mathrm{II}}^{(m)} = 10^{-4}$ (left) and $C_{\mathrm{I}}^{(m)} = 10^{-6}$, $C_{\mathrm{II}}^{(m)} = 10^{-4}$ (right) **b** Crack propagation rate $\mathrm{d}a/\mathrm{d}N$ vs. strain-energy release rate G for fiber-epoxy T300/914C (left) and AS4/PEEK (right) composites

microstructure and applying reduced-order approximation result in reduced-order microstructural equilibrium equation Eq. 2, where the corresponding coefficient tensors consist of integration of influence functions, nonlocal weight functions and elastic moduli:

$$\mathbf{C}^{(\alpha)} := \int_{S_\alpha} \nu^{(\alpha)}\left(\hat{\mathbf{y}}\right)\mathbf{C}\left(\hat{\mathbf{y}}\right) d\hat{\mathbf{y}} \tag{A.4}$$

$$\mathbf{C}\left(\hat{\mathbf{y}}\right) := \int_{\Theta} \mathbf{g}_\alpha\left(\mathbf{y},\hat{\mathbf{y}}\right) : \mathbf{L}\left(\mathbf{y}\right) : \mathbf{A}\left(\mathbf{y}\right) d\mathbf{y} \tag{A.5}$$

$$\mathbf{D}^{(\alpha\beta)} := -\int_{S_\alpha} \nu^{(\alpha)}\left(\hat{\mathbf{y}}\right)\mathbf{D}^{(\beta)}\left(\hat{\mathbf{y}}\right) d\hat{\mathbf{y}} \tag{A.6}$$

$$\mathbf{D}^{(\alpha)}\left(\hat{\mathbf{y}}\right) := \int_{\Theta} \mathbf{g}_\alpha\left(\mathbf{y},\hat{\mathbf{y}}\right) : \mathbf{L}\left(\mathbf{y}\right) : \mathbf{R}^{(\alpha)}\left(\mathbf{y}\right) d\mathbf{y} \tag{A.7}$$

$$\mathbf{R}^{(\alpha)}\left(\mathbf{y}\right) := \int_{S_\alpha} N^{(\alpha)}\left(\hat{\mathbf{y}}\right)\mathbf{g}_\alpha\left(\mathbf{y},\hat{\mathbf{y}}\right) d\hat{\mathbf{y}} \tag{A.8}$$

where $\mathbf{L}$ is the elastic moduli tensor varying with different material constituents. $\mathbf{A} = \mathbf{I}+\mathbf{G}$, $\mathbf{I}$ is the fourth order identity tensor, $\mathbf{G} = \nabla^s_{\mathbf{y}}\mathbf{H}$ is the elastic polarization tensor, and $\mathbf{g}_\alpha = \nabla^s_{\mathbf{y}}\mathbf{h}_\alpha$ stands for the separation polarization tensor.

Macroscopic stress-strain relationship Eq. 1 is obtained by averaging the stress field over microstructure domain. Coefficient tensor $\mathbf{Z}^{(\alpha)}$ is expressed as:

$$\mathbf{Z}^{(\alpha)} := \left\langle \mathbf{L}\left(\mathbf{y}\right) : \mathbf{R}^{(\alpha)}\left(\mathbf{y}\right)\right\rangle_{\Theta} \tag{A.9}$$

$$\bar{\mathbf{L}} := \left\langle \mathbf{L}\left(\mathbf{y}\right) : \mathbf{A}\left(\mathbf{y}\right)\right\rangle_{\Theta} \tag{A.10}$$

Systems of equations for temporal multiscale scheme

Figure 18 provides the summary of the system of equations for microchronological and macrochronological problems. The equations of the two scale problems have the same form, but the response fields are expressed in terms of different time scale coordinates. t represents macrochronological time resolving the whole structure life, where $t \in [0, t_{\mathrm{f}}]$. τ stands for microchorological time coordinates defined within the unit cyclic loading, where $\tau \in [0, \tau_0]$. The response field in macrochronological problem is homogenized using fixed-point operator: $\widetilde{\phi}\left(t\right) = \phi\left(t, \tau_0\right)$ [26]. In this work, the fixed point is chosen at the end of microchronological step.

Temporal local periodicity is not feasible in the microchronological problem due to the presence of irreversible damage condition. Therefore, almost periodicity is introduced for fatigue damage by allowing small value change within the microchronological time domain [26]. The derivative of temporal homogenized fatigue damage in the macrochronological problem is then expressed as follows according to the chain rule:

$$\widetilde{\dot{\omega}}^{(\alpha)}_{f,t}(t) = f(\boldsymbol{\delta}^{(\alpha)}, \dot{\boldsymbol{\delta}}^{(\alpha)}) + \dot{\omega}^{(\alpha)}_{f-\mathrm{ap}}(t) \tag{A.11}$$

where $f(\boldsymbol{\delta}^{(\alpha)}, \dot{\boldsymbol{\delta}}^{(\alpha)})$ stands for partial derivative of damage with respect to the coarse time scale t, $\dot{\omega}^{(\alpha)}_{f-\mathrm{ap}}(t)$ is the almost

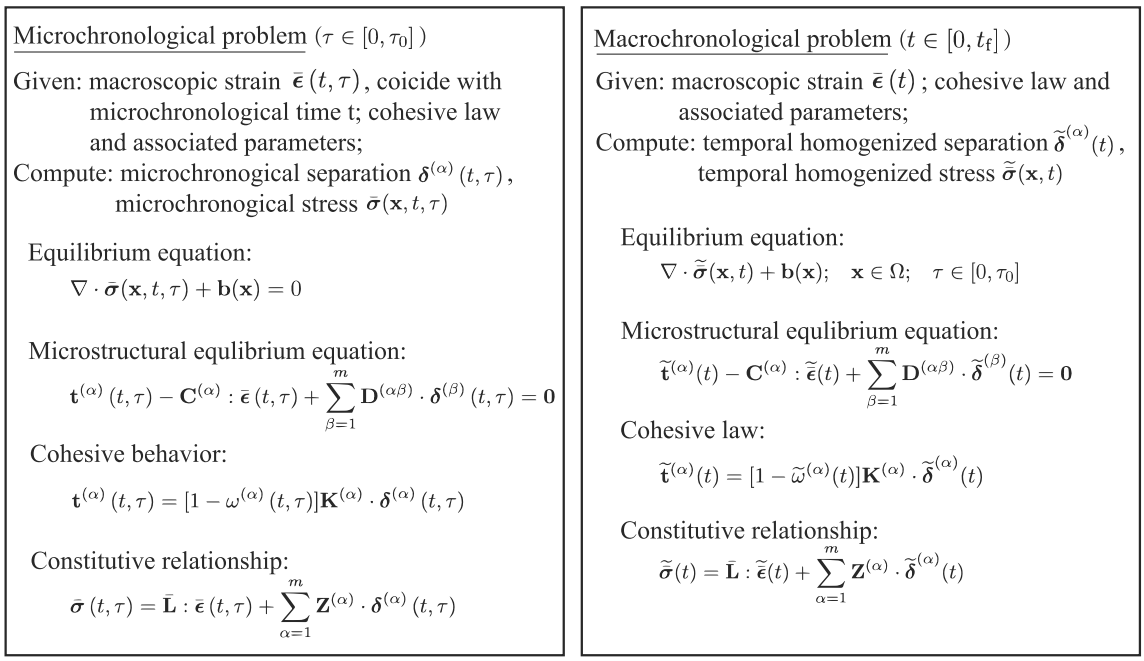

Fig. 18 Summary of microchronological and macrochronological problems based on temporal multiscale scheme

periodicity variable expressed as:

$$\dot{\omega}^{(\alpha)}_{f-\mathrm{ap}}(t) = \frac{1}{\tau_0}(\omega^{(\alpha)}_f(t,\tau_0) - \omega^{(\alpha)}_f(t,0)) \tag{A.12}$$

In adaptive macrochronological time stepping strategy, the time increment $\Delta t_i = t_{i+1} - t_i$ at the i^{th} macrochronological step is determined by:

$$\Delta t_i = \frac{\Delta\omega_p}{\|\boldsymbol{\omega}'_f(t_i)\|_\infty} \tag{A.13}$$

where $\boldsymbol{\omega}'_f(t_i)$ is the vector consisting of $\dot{\omega}^{(\alpha)}_{f-\mathrm{ap}}(t)$, which is evaluated in the current micro-chronological load cycle associated with all the failure path at all integration points within the macroscopic discretized domain. $\Delta\omega_p$ stands for the tolerance parameter for allowable damage accumulation across the macro-chronological time step.

References

1. Spearing SM, Beaumont PW (1992) Fatigue damage mechanics of composite materials Part III: prediction of post-fatigue strength. Compos Sci Technol 44(4):299–307. https://doi.org/10.1016/0266-3538(92)90067-D
2. Spearing SM, Beaumont PW, Smith PA (1992) Fatigue damage mechanics of composite materials Part IV: prediction of post-fatigue stiffness. Compos Sci Technol 44(4):309–317. https://doi.org/10.1016/0266-3538(92)90068-E
3. Krueger R (2002) The virtual crack closure technique: history, approach and applications. Tech. rep
4. Deobald L, Mabson G, Dopker B, Hoyt D, Baylor J, Graesser D (2007) Interlaminar fatigue elements for crack growth based on virtual crack closure technique. In: 48th AIAA/ASME/ASCE/AHS/ASC structures, structural dynamics, and materials conference, American Institute of Aeronautics and Astronautics, Reston, Virigina, vol 5, pp 4656–4663, https://doi.org/10.2514/6.2007-2091
5. Carvalho D, Ratcliffe JG, Chen BY, Pinho ST, Baiz PM, Tay TE (2014) Modeling quasi-static and fatigue-driven delamination migration. Tech. rep, NASA
6. Jimenez S, Duddu R (2016) On the parametric sensitivity of cohesive zone models for high-cycle fatigue delamination of composites. Int J Solids Struct 82:111–124. https://doi.org/10.1016/j.ijsolstr.2015.10.015
7. Turon A, Costa J, Camanho PP, Dávila CG (2007) Simulation of delamination in composites under high-cycle fatigue. Compos Part A Appl Sci Manuf 38(11):2270–2282. https://doi.org/10.1016/j.compositesa.2006.11.009
8. Nixon-Pearson OJ, Hallett SR, Harper PW, Kawashita LF (2013) Damage development in open-hole composite specimens in fatigue. Part 2: Numerical modelling. Compos Struct https://doi.org/10.1016/j.compstruct.2013.05.019
9. Yashiro S, Okabe T (2009) Numerical prediction of fatigue damage progress in holed CFRP laminates using cohesive elements. J Solid Mech Mater Eng 3(11):1212–1221. https://doi.org/10.1299/jmmp.3.1212
10. Okabe T, Yashiro S (2012) Damage detection in holed composite laminates using an embedded FBG sensor. Compos Part A Appl Sci Manuf 43(3):388–397. https://doi.org/10.1016/j.compositesa.2011.12.009
11. Iarve EV, Hoos K, Braginsky M, Zhou E, Mollenhauer DH (2017) Progressive failure simulation in laminated composites under fatigue loading by using discrete damage modeling. J Compos Mater 51(15):2143–2161. https://doi.org/10.1177/0021998316681831
12. Shi J, Chopp D, Lua J, Sukumar N, Belytschko T (2010) Abaqus implementation of extended finite element method using a level set representation for three-dimensional fatigue crack growth and life predictions. Eng Fract Mech 77(14):2840–2863. https://doi.org/10.1016/j.engfracmech.2010.06.009
13. Wang C, Xu X (2016) An extended phantom node method study of crack propagation of composites under fatigue loading. Compos Struct 154:410–418. https://doi.org/10.1016/j.compstruct.2016.07.022
14. (2015) Direct method for life prediction of fibre reinforced polymer composites based on kinematic of damage potential. Int J Fatigue 70:289–296, https://doi.org/10.1016/j.ijfatigue.2014.10.004
15. Xu J, Lomov SV, Verpoest I, Daggumati S, Van Paepegem W, Degrieck J (2015) A progressive damage model of textile composites on meso-scale using finite element method: fatigue damage analysis. Comput Struct 152:96–112. https://doi.org/10.1016/j.compstruc.2015.02.005
16. Van Paepegem W, Degrieck J (2002) Coupled residual stiffness and strength model for fatigue of fibre-reinforced composite materials. Compos Sci Technol 62(5):687–696. https://doi.org/10.1016/S0266-3538(01)00226-3
17. Kirane K, Bažant ZP (2015) Microplane damage model for fatigue of quasibrittle materials: sub-critical crack growth, lifetime and residual strength. Int J Fatigue 70:93–105. https://doi.org/10.1016/j.ijfatigue.2014.08.012
18. Wilt TE, Arnold SM, Saleeb AF (1997) A Coupled/uncoupled computational scheme for deformation and fatigue damage analysis of unidirectional metal-matrix composites. ASTM Special Tech Publ 1315:65–82
19. Mohammadi B, Fazlali B, Salimi-Majd D (2017) Development of a continuum damage model for fatigue life prediction of laminated composites. Compos Part A Appl Sci Manuf 93:163–176. https://doi.org/10.1016/j.compositesa.2016.11.021
20. Fang E, Cui X, Lua J (2017) A continuum damage and discrete crack-based approach for fatigue response and residual strength prediction of notched laminated composites. J Compos Mater 51(15):2203–2225. https://doi.org/10.1177/0021998317705975
21. Naghipour P, Pineda EJ, Bednarcyk BA, Arnold SM, Waas AM (2017) Fatigue analysis of notched laminates: a time-efficient macro-mechanical approach. J Compos Mater 51(15):2163–2180. https://doi.org/10.1177/0021998316668569
22. Fazlali B, Mohammadi B (2019) A microscale energy-based fatigue damage model for unidirectional composites under multiaxial loading at different stress ratios. Eng Fract Mech 205(November 2018):120–135. https://doi.org/10.1016/j.engfracmech.2018.11.024
23. Bogdanor MJ, Oskay C (2016) Prediction of progressive damage and strength of IM7/977-3 composites using the Eigendeformation-based homogenization approach: Static loading. J Compos Mater 51(10):1455–1472. https://doi.org/10.1177/0021998316650982
24. Oskay C, Fish J (2007) Eigendeformation-based reduced order homogenization for failure analysis of heterogeneous materials. Comput Methods Appl Mech Eng 196(7):1216–1243. https://doi.org/10.1016/j.cma.2006.08.015
25. Oskay C, Su Z, Kapusuzoglu B (2020) Discrete eigenseparation-based reduced order homogenization method for failure modeling of composite materials. Comput Methods Appl Mech Eng 359:112656. https://doi.org/10.1016/J.CMA.2019.112656

26. Crouch R, Oskay C, Clay S (2013) Multiple spatio-temporal scale modeling of composites subjected to cyclic loading. Comput Mech 51(1):93–107. https://doi.org/10.1007/s00466-012-0707-9
27. Crouch R, Oskay C (2015) Accelerated time integrator for multiple time scale homogenization. Int J Numer Methods Eng 101(13):1019–1042. https://doi.org/10.1002/nme.4863
28. Bogdanor MJ, Oskay C (2017) Prediction of progressive fatigue damage and failure behavior of IM7/977-3 composites using the reduced-order multiple space-time homogenization approach. J Compos Mater 51(15):2101–2117. https://doi.org/10.1177/0021998316665683
29. Bogdanor MJ, Clay SB, Oskay C (2019) Interacting damage mechanisms in laminated composites subjected to high amplitude fatigue. J Eng Mech 145(10):1–11. https://doi.org/10.1061/(ASCE)EM.1943-7889.0001655
30. Paulson WJ, Oskay C (2017) Failure prediction of countersunk composite bolted joints using reduced order multiple space-time homogenization. In: 32nd Technical Conference of the American Society for Composites 2017, https://doi.org/10.12783/asc2017/15230
31. Rots JG, Nauta P, Kusters GM, Blaauwendraad J (1985) Smeared crack approach and fracture localization in concrete. Heron 30(1)
32. Peerlings RHJ, Brekelmans WAM, de Borst R, Geers MGD (2000) Gradient-enhanced damage modelling of high-cycle fatigue. Int J Numer Methods Eng 49(12):1547–1569. https://doi.org/10.1002/1097-0207(20001230)49:123<1547::AID-NME16>3.0.CO;2-D
33. Fish J, Oskay C (2005) A nonlocal multiscale fatigue model. Mech Adv Mater Struct 12(6):485–500. https://doi.org/10.1080/15376490500259319
34. Guedes JM, Noboru K (1990) Preprocessing and postprocessing for materials based on the homogenization method with adaptive finite element methods. Comput Methods Appl Mech Eng 83(2):143–198. https://doi.org/10.1016/0022-2836(73)90435-X
35. Geers MGD, Kouznetsova VG, Matouš K, Yvonnet J (2017) Homogenization Methods and Multiscale Modeling: Nonlinear Problems. Encyclopedia of Computational Mechanics Second Edition pp 1–34, https://doi.org/10.1002/9781119176817.ecm2107
36. Camanho PP, Dávila CG (2002) Mixed-mode decohesion finite elements for the simulation of delamination in composite materials. Tech. rep, NASA
37. Bažant ZP, Oh BH (1983) Crack band theory for fracture of concrete. Matériaux et Constructions 16(3):155–177. https://doi.org/10.1007/BF02486267
38. Khoramishad H, Crocombe AD, Katnam KB, Ashcroft IA (2010) Predicting fatigue damage in adhesively bonded joints using a cohesive zone model. Int J Fatigue 32(7):1146–1158. https://doi.org/10.1016/j.ijfatigue.2009.12.013
39. Benzeggagh ML, Kenane M (1996) Measurement of mixed-mode delamination fracture toughness of unidirectional glass/epoxy composites with mixed-mode bending apparatus. Compos Sci Technol 56(4):439–449. https://doi.org/10.1016/0266-3538(96)00005-X
40. Kenane M, Benzeggagh M (1997) Mixed-mode delamination fracture toughness of unidirectional glass/epoxy composites under fatigue loading. Compos Sci Technol 57(5):597–605. https://doi.org/10.1016/S0266-3538(97)00021-3
41. Spearing SM, Beaumont PW (1992) Fatigue damage mechanics of composite materials. I: Experimental measurement of damage and post-fatigue properties. Compos Sci Technol 44(2):159–168, https://doi.org/10.1016/0266-3538(92)90109-G
42. Ambu R, Aymerich F, Bertolino F (2005) Investigation of the effect of damage on the strength of notched composite laminates by digital image correlation. J Strain Anal Eng Des 40(5):451–461. https://doi.org/10.1243/030932405X16106
43. Wang CM, Shin CS (2002) Residual properties of notched [0/90]4S AS4/PEEK composite laminates after fatigue and reconsolidation. Compos B Eng 33(1):67–76. https://doi.org/10.1016/S1359-8368(01)00049-X
44. König M, Krüger R, Kussmaul K, von Alberti M, Gädke M (1997) Characterizing static and fatigue interlaminar fracture behavior of a first generation graphite/epoxy composite. ASTM Int. https://doi.org/10.1520/stp18270s
45. Martin R, Murri G (1990) Characterization of Mode I and Mode II delamination growth and thresholds in AS4/PEEK composites. ASTM Int. https://doi.org/10.1520/stp24115s